IEEE Transactions on Robotics (T-RO) paper, presented at ICRA 2024, Yokohama, Japan. Cite as T-RO paper.

Simultaneous Localization and Actuation Using Electromagnetic Navigation Systems

Denis von Arx, Cedric Fischer, Harun Torlakcik, Salvador Pané, Bradley J. Nelson, *Fellow, IEEE* and Quentin Boehler, *Member, IEEE,*

***Abstract*—Remote magnetic navigation provides a promising approach for improving the maneuverability and safety of surgical tools, such as catheters and endoscopes, in complex anatomies. The lack of existing localization systems compatible with this modality, beyond fluoroscopy and its harmful ionizing radiation, impedes its translation to clinical practice. To address this challenge, we propose a localization method that achieves full pose estimation by superimposing oscillating magnetic fields for localization onto actuation fields generated by an electromagnetic navigation system. The resulting magnetic field is measured using a three-axis magnetic field sensor embedded in the magnetic device to be localized. The method is evaluated on a three-coil system, and simultaneous actuation and localization is demonstrated with a magnetic catheter prototype with a Hall-effect sensor embedded at its tip. We demonstrate position estimation with mean accuracy and precision below 1 mm, and orientation estimation with mean errors below 2° at 10 Hz in a workspace of 80 × 80 × 60 mm. This contribution aims to advance the clinical adoption of remote magnetic navigation in minimally invasive surgery.**

***Index Terms*—Remote magnetic navigation, localization, Hall-effect sensor, electromagnetic tracking, medical robotics**

NOMENCLATURE

M	Number of electromagnets
$i^{\mathrm{a}}_m, i^{l}_m$	Actuation and localization current in electromagnet m
$\underline{i}_m$	Phasor of localization current in electromagnet m in $\mathbb{C}$
f_m	Oscillation frequency of localization current in electromagnet m
$\mathbf{i}^{\mathrm{a}}$	Actuation current vector in $\mathbb{R}^M$
$\underline{\mathbf{i}}^{l}$	Localization current phasor vector in $\mathbb{C}^M$
$\mathbf{b}^{\mathrm{a}}(\mathbf{p}, t)$	Actuation field in $\mathbb{R}^3$ at position $\mathbf{p}$ and time t
$\mathbf{b}^{l}(\mathbf{p}, t)$	Localization field in $\mathbb{R}^3$ at position $\mathbf{p}$ and time t
$\underline{\mathbf{b}}_m$	Magnetic field phasor vector of frequency f_m in $\mathbb{C}^3$
$\mathcal{K}_0, \mathcal{K}_{\mathrm{s}}, \mathcal{K}_r$	Coordinate system of eMNS, device sensor and reference sensor
$\hat{\underline{\mathbf{b}}}_m$	Estimate of magnetic field phasor vector at sensor location
$[\hat{\underline{\mathbf{b}}}_m]_{\mathcal{K}_{\mathrm{s}}}$	Matrix of magnetic field phasor estimates in $\mathbb{C}^{3\times M}$ expressed in $\mathcal{K}_{\mathrm{s}}$
$\breve{\underline{\mathbf{b}}}_m(\mathbf{p}, \mathbf{i}^{\mathrm{a}})$	Magnetic phasor field prediction
$\lvert\underline{\mathbf{b}}_m\rvert(\mathbf{p}, \mathbf{i}^{\mathrm{a}})$	Magnetic phasor magnitude field prediction
T_{seq}	Acquisition duration of a measurement sequence
$\boldsymbol{\mathcal{b}}_{s_i}$	Sequence in $\mathbb{R}^{N_s}$ of N_s magnetic field measurements in sensor direction s_i
$\boldsymbol{\mathcal{b}}^{\mathrm{a}}_{s_i}$,$\hat{\boldsymbol{\mathcal{b}}}^{\mathrm{a}}_{s_i}$	Actuation field contribution to measurement sequence and its estimate in $\mathbb{R}^{N_s}$
$\boldsymbol{\mathcal{b}}^{l}_{s_i}$,$\hat{\boldsymbol{\mathcal{b}}}^{l}_{s_i}$	Localization field contribution to measurement sequence and its estimate in $\mathbb{R}^{N_s}$
H	Number of base sequences used for approximation of $\boldsymbol{\mathcal{b}}^{\mathrm{a}}_{s_i}$
$\boldsymbol{f}^{\mathrm{a}}_h$	h-th base sequence of length N_s in $\mathbb{R}^{N_s}$
$\boldsymbol{\mathcal{b}}_{r_i}$	Sequence in $\mathbb{R}^{N_s}$ of N_s magnetic field measurements in reference sensor direction r_i
$\hat{\underline{\mathbf{b}}}^{r}_m$	Estimate of magnetic field phasor vector at reference sensor position
$g_i(\mathbf{p})$	Localization gradient at $\mathbf{p}$ in direction e_i

I. INTRODUCTION

REMOTE magnetic navigation (RMN) is a method for remotely steering devices containing magnetizable material using magnetic fields [1]. This modality is particularly promising for minimally invasive surgery, as forces and torques are directly applied to the tip of soft instruments such as catheters [2]. This increases their dexterity and allows for safe navigation in complex anatomies [3]–[5]. RMN also allows for increased automation of surgical procedures, including minimally invasive endovascular interventions [4].

In this context, accurate and precise position and orientation feedback is crucial. Fluoroscopic imaging is commonly used to continuously track surgical instruments intra-operatively [6] despite the known adverse health effects of this imaging modality. An alternative to this modality is to localize the instrument using magnetic field measurements. For this purpose, magnetic tracking systems are commercially available. However, these systems are not compatible with magnetic actuation systems which cause distortions of the fields used for localization. Recent works using Hall effect sensors and electromagnets for localization of surgical tools have been reported in [7]–[9], but they use systems that are not designed for actuation purposes.

Coupled magnetic actuation and localization have received significant research attention. Di Natali et al. developed a method for 6 degree-of-freedom (DOF) pose detection using multiple Hall sensors, and an inertial measurement unit (IMU) for wireless capsule endoscopy that is compatible with permanent magnet actuation [10], [11]. 6-DOF localization

The authors are with the Multi-Scale Robotics Lab, ETH Zurich, Switzerland.

Manuscript received June 9, 2023; revised October 12, 2023.

IEEE Transactions on Robotics (T-RO) paper, presented at ICRA 2024, Yokohama, Japan. Cite as T-RO paper.

with Hall effect sensors was also demonstrated in a system using rotating magnetic dipole fields that could also be used to actuate a magnetic capsule [12]. The combination of Hall effect sensors and IMUs to provide a pose estimate has further been considered in [13], [14]. A method for simultaneous localization and actuation with Hall sensors and an IMU that utilizes both dynamic magnetic fields and static magnetic fields from permanent magnets for actuation was presented in [15]. Son et al. presented a 5-DOF localization technique using a 2D Hall sensor array that measures the magnetic field of a permanent magnet under actuation which was also used for capsule endoscope applications [16], [17].

Although these works provide relevant approaches and offer unique advantages for their respective applications, their adaptation to small tethered devices such as endoscopes, guidewires or catheters still suffers from several limitations. These methods either rely on the combination of several sensors (which impedes their miniaturization and integration into aforementioned devices), they do not provide localization and actuation simultaneously, or they rely on sensing the magnetic field of the magnet to be actuated which may not be compatible with smaller magnets, localization over larger distances, or applications where 6-DOF localization is required such as for tethered endoscopes.

In certain applications, the magnetic object to be actuated can also be continuous, such as magnetic continuum robots [18], or the localization of multiple sensors within the workspace may be required. The use of constant magnetic field gradients generated by an electromagnetic navigation system (eMNS) to localize magnetic devices using a single three-axis Hall sensor was investigated in [19], [20]. However, using a constant magnetic field and the measurement of a single magnetic sensor is not enough to determine its pose without incurring additional geometric constraints or applying changing magnetic fields, both being detrimental to a simultaneous actuation.

To address these limitations, this paper introduces a method which uses magnetic fields to simultaneously actuate and localize with 6-DOF a magnetically-guided, tethered device such as a catheter, endoscope or guidewire with the same set of electromagnets, and without any additional geometrical assumptions. The actuation is achieved by steering the object in the desired direction using the magnetic field and advancing or retracting the object using an advancement mechanism. The method only requires a three-axis magnetic field sensor that can be implemented in a single integrated circuit, resulting in a significant reduction of the overall package size compared to existing methods. The principle of the method also allows for localization of multiple such sensors within the workspace of the eMNS. These contributions can help advance the clinical adoption of RMN in minimally invasive surgery. Simultaneous localization and actuation is achieved by adding small oscillating fields of distinct frequencies to the actuation field produced by each electromagnet in the eMNS. The method introduced in section II, relies on a successive position and orientation estimation of a single sensor which provides an *in-situ* measurement of the magnetic field at the pose to be determined (see Fig. 1). Localization accuracy is particularly impeded by the non-linear and dynamic behavior of the electromagnets. For this reason we also propose compensation methods for these effects, making our method applicable to a broad variety of systems. We evaluate our method experimentally using an eMNS composed of three electromagnets (see section III). We characterize the localization performance with and without the influence of an actuation field, and for various trajectories within the workspace of the system. We also demonstrate a realistic navigation task for a magnetic catheter in a flat vascular phantom, and show that we can precisely and accurately steer and estimate the pose of the magnetic tip to navigate the different branches of the model. We discuss our methods and results and conclude in section IV.

II. Method

A. Electromagnetic Navigation Systems

An eMNS is composed of M electromagnets that generate magnetic fields, which are controlled by the amount of electric current running through their conductive windings. The resulting magnetic field $\mathbf{b}$ generates a force $\mathbf{f}$ and a torque $\boldsymbol{\tau}$ on the magnetic object to be steered [2]:

$$\begin{aligned} \mathbf{f} &= \nabla(\mathbf{m} \cdot \mathbf{b}) \\ \boldsymbol{\tau} &= \mathbf{m} \times \mathbf{b} \end{aligned} \tag{1}$$

with $\mathbf{m}$ the magnetic moment of the object. An example of an eMNS composed of $M = 3$ electromagnets is depicted in Fig. 1a. In this work, we consider the actuation of an object by steering it into a certain direction using the magnetic field and advancing or retracting it in space using an advancement mechanism. The magnetic field $\mathbf{b}(\mathbf{p}, \mathbf{i})$ generated by an eMNS depends on the position $\mathbf{p}$ in space and on the currents $\mathbf{i}$ flowing in the electromagnets in the system. To actuate a magnetic object, these currents generate an *actuation field* $\mathbf{b}^{\mathrm{a}}(\mathbf{p})$ to produce a desired torque $\boldsymbol{\tau}^*$ or a desired force $\mathbf{f}^*$ on the object according to (1). These currents are referred to as *actuation currents* and denoted $\mathbf{i}^{\mathrm{a}} = \begin{bmatrix} i_1^{\mathrm{a}} & \cdots & i_M^{\mathrm{a}} \end{bmatrix}^T$. The method to compute $\mathbf{i}^{\mathrm{a}}$ depends on the navigation task to be performed. In [21], Kummer et al. show a method to compute $\mathbf{i}^{\mathrm{a}}(\mathbf{f}^*, \boldsymbol{\tau}^*)$ in terms of the desired torque and force on the object, whereas [22] shows a method to compute $\mathbf{i}^{\mathrm{a}}(\mathbf{b}^*, \mathbf{f}^*)$ in terms of the desired field at the location of the object and the desired force on the object. The method presented in this paper to simultaneously actuate and localize a magnetic object using an eMNS is generic. It is fully independent of the way that $\mathbf{i}^{\mathrm{a}}$ is computed and the navigation task to be performed.

B. Superposition of actuation and localization currents

The desired current $i_m^*(t)$, tracked by each electromagnet $m \in \{1, \ldots, M\}$ at time t using a dedicated control scheme, is set as the superposition of the actuation current $i_m^{\mathrm{a}}(t)$ and a so-called *localization current*, denoted $i_m^l(t)$, that is sinusoidally oscillating (see Fig. 1c):

$$i_m^*(t) = i_m^{\mathrm{a}}(t) + i_m^l(t) \tag{2}$$

with

$$i_m^l(t) = \mathrm{Re}\left(\underline{i}_m e^{j2\pi f_m t}\right) = I_m \cos(2\pi f_m t + \theta_m) \tag{3}$$

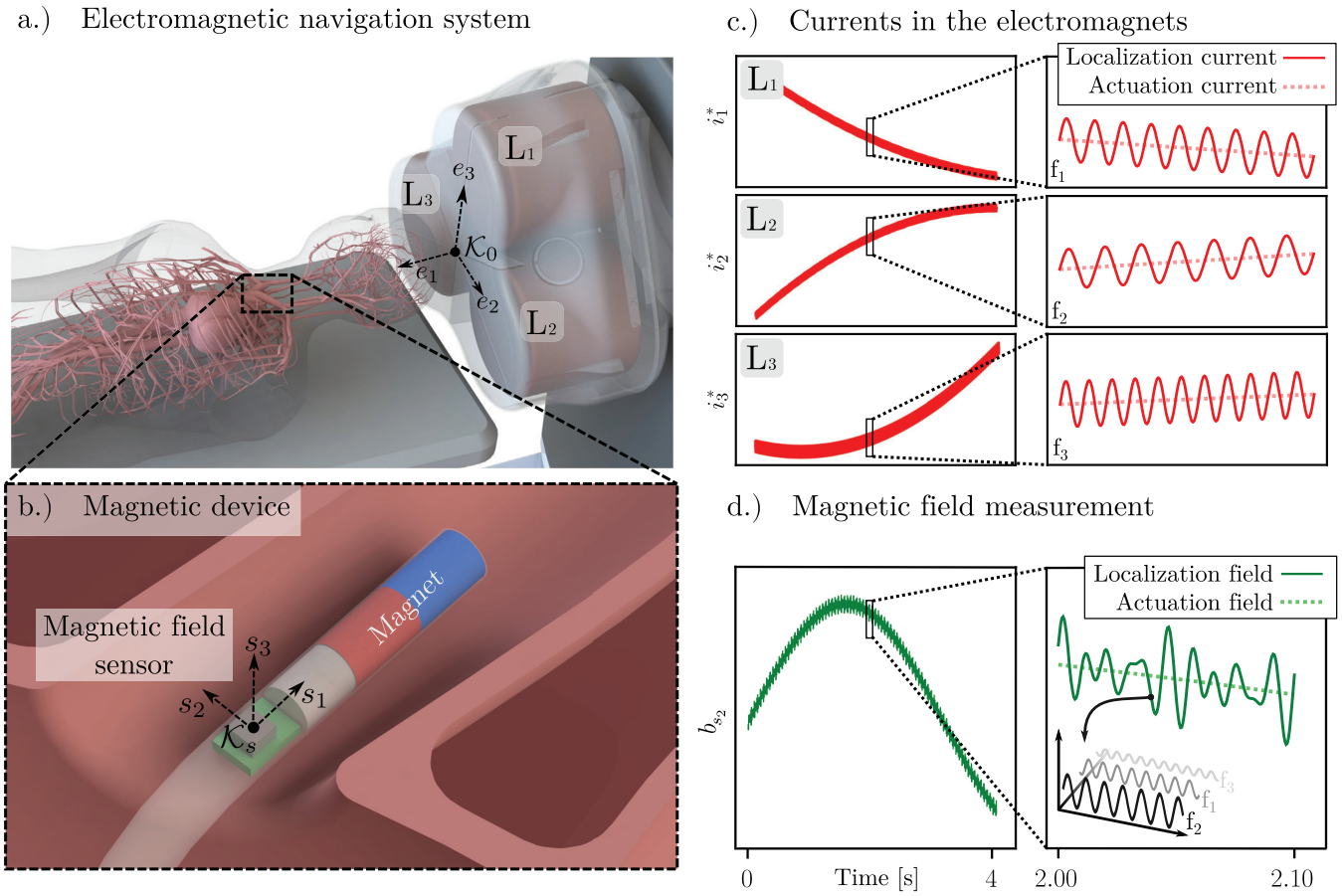

Fig. 1. Simultaneous actuation and localization with an eMNS for minimally invasive endovascular procedures. a.) eMNS composed of electromagnets L_1, L_2 and L_3 b.) Close-up of the catheter tip embedded with a 3-axis magnetic field sensor and a distal permanent magnet. c.) Currents in electromagnets consisting of a superposition of actuation and localization currents. The oscillation frequency f_m of the localization current is different for each electromagnet. d.) Magnetic field measurement of the component b_{s_2} of the magnetic field using the magnetic field sensor. The localization field can be decomposed in components of frequencies f_m.

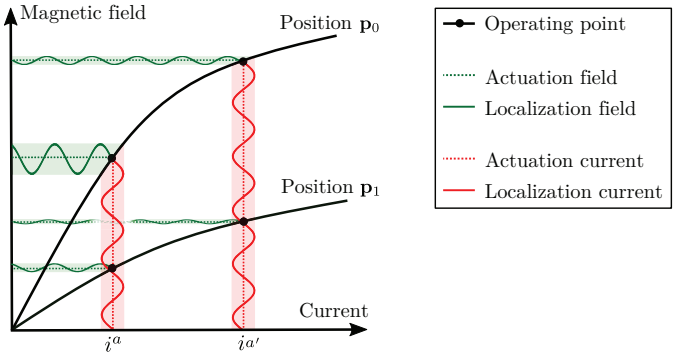

Fig. 2. Influence of position and actuation current on the localization field caused by a given localization current in a single electromagnet. A small oscillating localization current around two different actuation currents (i^a and $i^{a'}$) results in oscillations of the localization field around the actuation field through the magnetic response of the electromagnet (black lines). The response depends on the position (here $\mathbf{p}_0$ or $\mathbf{p}_1$) and the actuation current, due to the magnetic saturation occurring in the electromagnet.

The complex number $\underline{i}_m = I_m e^{j\theta_m}$ is a phasor comprising the phase θ_m and amplitude I_m of the localization current, and f_m denotes its oscillation frequency. The localization currents create oscillations of the magnetic field around the actuation field at the frequencies f_m as depicted in Fig. 1d, so that

$$\mathbf{b}(\mathbf{p},t) = \mathbf{b}^{\mathrm{a}}(\mathbf{p},t) + \mathbf{b}^{l}(\mathbf{p},t) \tag{4}$$

where $\mathbf{b}^l(\mathbf{p},t)$, referred to as the *localization field*, describes the magnetic field oscillations caused by the localization currents at position $\mathbf{p}$ and time t (see Figures 1d and 2). The magnetic field $\mathbf{b}(\mathbf{p},t)$ is measured by a sensor integrated in the device to be localized (see Fig. 1b and d). The amplitudes I_m of the localization currents are chosen sufficiently small and the frequencies f_m sufficiently high such that the resulting localization field does not cause an appreciable motion of the actuated object. How much motion of the actuated object is tolerable as a result of the localization field depends on the intended application. Within the scope of this work, the frequencies and amplitudes were chosen in such a way that the motion of a test catheter, presented in Section III-F, was an order of magnitude smaller than the precision resulting from the localization method. It is assumed initially that the actuation currents are quasi-stationary compared to the localization currents. Since the amplitudes of the localization currents are small, their superposition leads to a linear response in the magnetic field (see Fig. 2), and the localization field can then

be written as

$$\mathbf{b}^l(\mathbf{p},t) = \sum_m \mathrm{Re}\left(\underline{\mathbf{b}}_m(\mathbf{p},\mathbf{i}^{\mathrm{a}},\underline{\mathbf{i}}^l)e^{j2\pi f_m t}\right) \tag{5}$$

with $\underline{\mathbf{b}}_m = \begin{bmatrix} b_{m,e_1}e^{j\theta_{m,e_1}} & b_{m,e_2}e^{j\theta_{m,e_2}} & b_{m,e_3}e^{j\theta_{m,e_3}}\end{bmatrix}^T_{\mathcal{K}_0}$ a vector of phasors in $\mathbb{C}^3$ describing the amplitude and phase of oscillation of the components of the localization field of oscillation frequency f_m and expressed in a coordinate system $\mathcal{K}_0$ of standard basis vectors $\{\mathbf{e}_1,\mathbf{e}_2,\mathbf{e}_3\}$ fixed to the eMNS (see Fig. 1a). The vector $\underline{\mathbf{b}}_m(\mathbf{p},\mathbf{i}^{\mathrm{a}},\underline{\mathbf{i}}^l)$ depends on the position in space and the localization current phasors $\underline{\mathbf{i}}^l = \begin{bmatrix}\underline{i}_1 & \cdots & \underline{i}_M\end{bmatrix}^T \in \mathbb{C}^M$. It also depends on the actuation currents $\mathbf{i}^{\mathrm{a}} \in \mathbb{R}^M$ due to magnetic saturation occurring in the electromagnet cores [1] as illustrated in Fig. 2. Note that in the notation for the phasor vector of the localization field $\underline{\mathbf{b}}_m$ and the phasor of the localization current $\underline{i}_m$ the localization superscript l is omitted. The l superscript is implicitly assumed for all phasor quantities.

C. Localization method

1) Principle: For an eMNS composed of more than two distinct electromagnets ($M > 2$), each pose in its workspace is characterized by a unique combination of M vectors of phasors $\underline{\mathbf{b}}_1,\ldots,\underline{\mathbf{b}}_M$ generated by the electromagnets. The principle of the localization method proposed here consists of measuring these phasors at the pose to be determined with an embedded magnetic sensor resulting in an estimate of the phasors at the location of the sensor:

$$[\hat{\underline{\mathbf{b}}}_m]_{\mathcal{K}_{\mathrm{s}}} = \left[\hat{\underline{\mathbf{b}}}_1 \cdots \hat{\underline{\mathbf{b}}}_M\right]_{\mathcal{K}_{\mathrm{s}}} = \begin{bmatrix} \hat{\underline{b}}_{1,s_1} & \cdots & \hat{\underline{b}}_{M,s_1} \\ \hat{\underline{b}}_{1,s_2} & \cdots & \hat{\underline{b}}_{M,s_2} \\ \hat{\underline{b}}_{1,s_3} & \cdots & \hat{\underline{b}}_{M,s_3} \end{bmatrix}_{\mathcal{K}_{\mathrm{s}}} \tag{6}$$

where $[\hat{\underline{\mathbf{b}}}_m]_{\mathcal{K}_{\mathrm{s}}} \in \mathbb{C}^{3\times M}$ refers to a matrix composed of the M estimated vectors of phasors. The elements $\hat{\underline{b}}_{m,s_i}$ of this matrix are the coordinates of the vector $\hat{\underline{\mathbf{b}}}_m$ along the axes s_i of the sensor frame $\mathcal{K}_{\mathrm{s}}$ (Fig. 1b). They correspond to the phasors of the localization field produced by each electromagnet m along each direction s_i . Each vector $\hat{\underline{\mathbf{b}}}_m$ and its magnitude $|\hat{\underline{\mathbf{b}}}_m|$ for $m \in \{1,\ldots,M\}$ are respectively compared to a prediction of the phasor fields and phasor magnitude fields present in the workspace of the eMNS:

$$\breve{\underline{\mathbf{b}}}_m(\mathbf{p},\mathbf{i}^{\mathrm{a}}) \tag{7a}$$

$$|\breve{\underline{\mathbf{b}}}_m|(\mathbf{p},\mathbf{i}^{\mathrm{a}}) \tag{7b}$$

These predictions are known by calibration in $\mathcal{K}_0$. Note that in the above expressions, we omitted the dependency on $\underline{\mathbf{i}}^l$ since the localization current phasors are kept constant. The dependency on $\mathbf{i}^{\mathrm{a}}$ is kept in the notation, since the actuation currents change over time and influence the localization fields. The pose of the sensor is characterized by its position and its orientation which is described by the rotation matrix $\mathbf{R}$ from $\mathcal{K}_{\mathrm{s}}$ to $\mathcal{K}_0$. An estimate for the sensor position $\hat{\mathbf{p}}$ in $\mathcal{K}_0$, and an estimate for the sensor orientation $\hat{\mathbf{R}}$ is obtained in two steps, by first estimating the position and then using the position estimate to estimate the orientation:

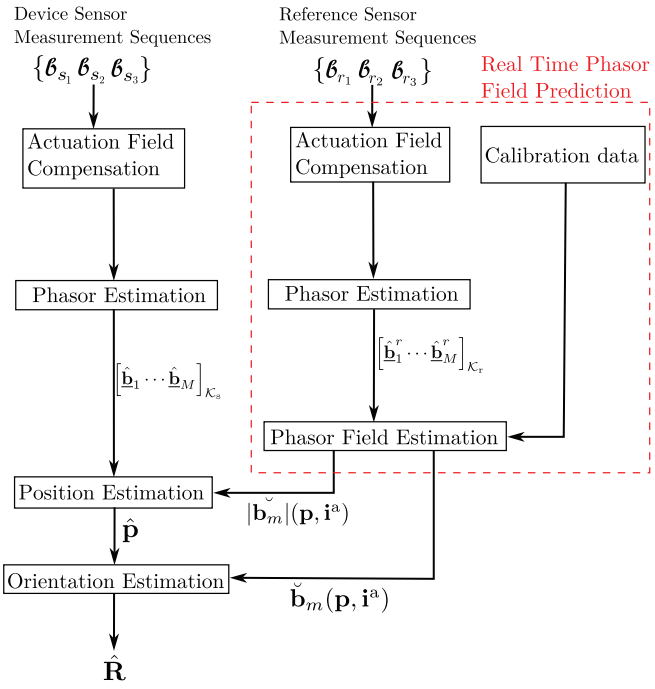

Fig. 3. Schematic overview of the pose estimation

$$\hat{\mathbf{p}} = \underset{\mathbf{p}}{\mathrm{argmin}} \sum_m \left(|\hat{\underline{\mathbf{b}}}_m| - |\breve{\underline{\mathbf{b}}}_m|(\mathbf{p},\mathbf{i}^{\mathrm{a}})\right)^2 \tag{8a}$$

$$\hat{\mathbf{R}} = \underset{\mathbf{R}\in SO(3)}{\mathrm{argmin}} \left\| \mathbf{R}[\hat{\underline{\mathbf{b}}}_m]_{\mathcal{K}_{\mathrm{s}}} - [\breve{\underline{\mathbf{b}}}_m(\hat{\mathbf{p}},\mathbf{i}^{\mathrm{a}})]_{\mathcal{K}_0} \right\|_F \tag{8b}$$

A general overview of the localization method is depicted in Fig. 3. The magnetic field measurements, acquired in sequences of N_s samples for each sensor axis, are denoted by $\boldsymbol{\mathcal{b}}_{s_i}$ for each direction s_i of $\mathcal{K}_s$. The phasors introduced in (6) are estimated from $\boldsymbol{\mathcal{b}}_{s_i}$ following a compensation of the influence of the actuation field on these estimates. The phasor and phasor magnitude fields introduced in (7) can be predicted for any position $\mathbf{p}$ in the workspace $\mathcal{W} \subset \mathbb{R}^3$ of the eMNS. This prediction is performed in real time using data from an offline calibration procedure, and measurements from an additional reference sensor $\boldsymbol{\mathcal{b}}_{r_i}$ that is attached to a reference sensor coordinate system $\mathcal{K}_r$ placed near the electromagnets. The reference sensor phasor measurements $\hat{\underline{\mathbf{b}}}^r_m$ are used to predict the influence of the actuation currents on $\breve{\underline{\mathbf{b}}}_m(\mathbf{p},\mathbf{i}^{\mathrm{a}})$ and $|\breve{\underline{\mathbf{b}}}_m|(\mathbf{p},\mathbf{i}^{\mathrm{a}})$.

2) Magnetic phasor measurement: The vectors $\underline{\mathbf{b}}_m$ must be measured *in-situ*, at the position to be determined or calibrated. The coordinates of their estimates $\hat{\underline{\mathbf{b}}}_m$ are obtained using the discrete Fourier transform (DFT) of a sequence of N_s magnetic field measurements $\boldsymbol{\mathcal{b}}_{s_i} \in \mathbb{R}^{N_s}$ along each axis s_i of $\mathcal{K}_s$. This sequence is acquired over a so-called *measurement sequence* of duration T_{seq}, and regularly sampled over time with a three-axis magnetic sensor for each direction s_i (see Fig. 4a and b). The measurement sequence acquisition frequency, also referred to as the *localization frequency* in the

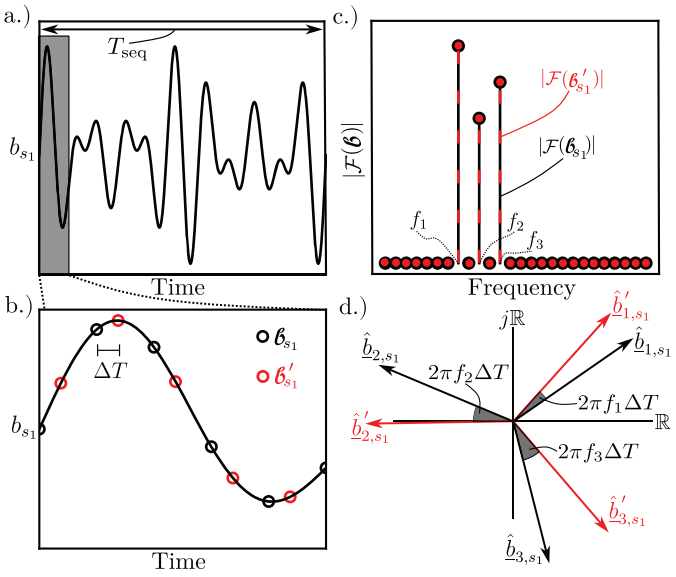

Fig. 4. Magnetic field measurement and phasor estimation with a magnetic field sensor. a.) Component b_{s_1} of the magnetic field over a measurement sequence of duration T_{seq}. b.) The sampling $\mathcal{b}_{s_1}$ of b_{s_1} starting at $t = 0$ (black points), and $\mathcal{b}'_{s_1}$ with a time delay at $t = \Delta T$ (red points). c.) The amplitudes of the measurements DFT are not affected by the delay, but d.) the delay causes a phase shift $2\pi f_m \Delta T$ on the measured phasors.

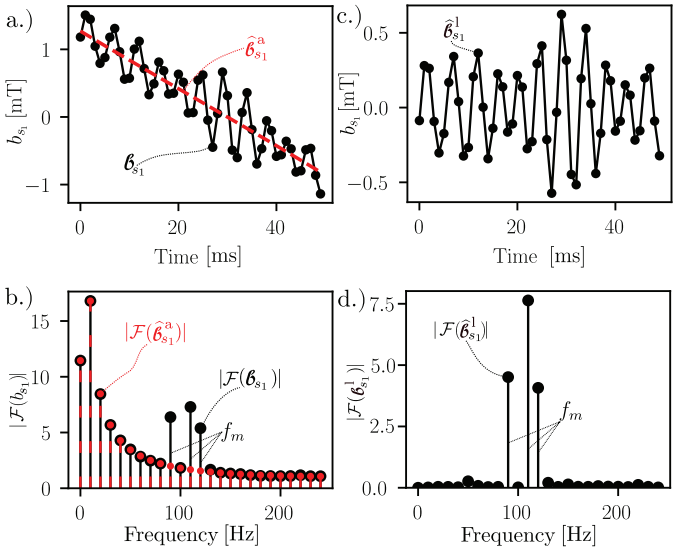

Fig. 5. Influence and compensation of a dynamic actuation field on the phasors estimation. a.) Magnetic field measurement sequence $\mathcal{b}_{s_1}$ and estimated actuation field sequence $\hat{\mathcal{b}}^{\text{a}}_{s_1}$ for component b_{s_1} sampled by sensor and b.) absolute values of their respective DFT components c.) Estimated localization field sequence $\hat{\mathcal{b}}^{l}_{s_1}$ and d.) absolute values of its DFT components.

following, is then denoted $f_{\text{seq}} := T_{\text{seq}}^{-1}$. The components $\hat{\underline{b}}_{m,s_i}$ of the phasor $\hat{\underline{\mathbf{b}}}_m$ in $\mathcal{K}_s$ (see (6)) are computed as

$$\hat{\underline{b}}_{m,s_i} = \frac{2}{N_s} \mathcal{F}(\mathcal{b}_{s_i})_{k_m} \tag{9}$$

where $\mathcal{F}(\mathcal{b}_{s_i})_{k_m}$ is the DFT of $\mathcal{b}_{s_i}$ evaluated at the discrete frequency $k_m := T_{\text{seq}} f_m$. The frequencies f_m of the localization currents are chosen as distinct integer multiples of f_{seq} such that k_m are distinct integer numbers. This also causes the localization currents to generate distinct peaks in the DFT of the magnetic field measurements (see Fig. 4c). Moreover, the magnetic localization field will then also be periodic with a period T_{seq}. The measurement of the phasors (9) depends on the time within T_{seq} when the sampling is started. Note that an acquisition delay ΔT causes a phase shift $2\pi f_m \Delta T$ on the measured components of $\underline{\mathbf{b}}_m$, while the measurement of their magnitude remains unaffected (see Fig. 4b and d). In order to obtain unique phasor measurements, the sampling of the magnetic field sensor should be synchronized with the generation of the localization currents.

3) Compensation for the actuation fields dynamics: The estimate of the phasors (9) assumes that the dynamics of the actuation field $\mathbf{b}^{\text{a}}$ can be neglected compared to the dynamics of the localization field $\mathbf{b}^{l}$. In other words, it assumes that $\mathbf{b}^{\text{a}}$ does not generate significant frequency components at the oscillation frequencies of the localization field. However, this assumption may not hold if the actuation field undergoes dynamic changes. During such a change in the actuation field, the estimation of the phasor using (9) is less reliable, and in turn, affects the precision and accuracy of the localization. An example of a measurement for the component b_{s_1} of the magnetic field during a dynamic change and its DFT are shown in Fig. 5a and b. Although the localization field produces distinct peaks at the discrete frequencies k_m in the DFT of the measurement, the actuation field significantly contributes to these DFT components. This introduces an error in the estimation of the localization field phasors based on this measurement.

We can think of the measurement sequence as being made up of a contribution from the actuation field and the localization field $\mathcal{b}_{s_i} = \mathcal{b}^{\text{a}}_{s_i} + \mathcal{b}^{l}_{s_i}$ with $\mathcal{b}_{s_i}, \mathcal{b}^{\text{a}}_{s_i}, \mathcal{b}^{l}_{s_i} \in \mathbb{R}^{N_s}$. We refer to $\mathcal{b}^{\text{a}}_{s_i}$ as the actuation field sequence and to $\mathcal{b}^{l}_{s_i}$ as the localization field sequence. In order to reduce errors due to dynamic actuation fields, we estimate the phasors from the DFT of a localization field sequence estimate $\hat{\mathcal{b}}^{l}_{s_i} \in \mathbb{R}^{N_s}$ as follows:

$$\hat{\underline{b}}_{m,s_i} = \frac{2}{N_s} \mathcal{F}(\hat{\mathcal{b}}^{l}_{s_i})_{k_m} \tag{10}$$

with

$$\hat{\mathcal{b}}^{l}_{s_i} = \mathcal{b}_{s_i} - \hat{\mathcal{b}}^{\text{a}}_{s_i} \tag{11}$$

The estimate of the localization field sequence $\hat{\mathcal{b}}^{l}_{s_i}$ is obtained by subtracting an estimate of the actuation field sequence $\hat{\mathcal{b}}^{\text{a}}_{s_i}$ from the initial measurement sequence. The result of this compensation is illustrated in Figure 5c, which shows the estimated $\hat{\mathcal{b}}^{l}_{s_i}$. Fig. 5d shows the DFT of this estimated localization field sequence, which illustrates a significant reduction of the frequency components contributed by the actuation field sequence.

To identify $\hat{\mathcal{b}}^{\text{a}}_{s_i}$ for each measurement sequence, we model it as a sum of H base sequences $\boldsymbol{f}^{\text{a}}_h \in \mathbb{R}^{N_s}$ of length N_s:

$$\mathbf{c}_i \hat{\mathcal{b}}^{\text{a}}_{s_i} = \sum_h c_{i,h} \boldsymbol{f}^{\text{a}}_h \tag{12}$$

where $\mathbf{c}_i = (c_{i,1}, \ldots, c_{i,H}) \in \mathbb{R}^H$ are real coefficients to be determined for every new measurement sequence. The base

sequences should be chosen such that they can adequately approximate the expected actuation field sequence within the time interval of a measurement sequence. Assuming that the localization field sequence produces frequency components only at k_m and associated, complex conjugate components at $N_s - k_m$, the DFT of the actuation field at any discrete frequency $k \neq \{k_1, \ldots, k_M, N_s - k_1, \ldots, N_s - k_M\}$ can be approximated as $\mathcal{F}(\boldsymbol{\mathcal{b}}_{s_i})_k$, since the contribution of the localization field sequence at these frequencies is zero. The coefficients in $\mathbf{c}_i$ are thus determined in the following manner at each new measurement sequence:

$$\mathbf{c}_i = \underset{\mathbf{c}}{\operatorname{argmin}} \left\| \mathcal{F}(\boldsymbol{\mathcal{b}}_{s_i})_{k \neq k_m} - \mathcal{F}({}^{\mathbf{c}}\hat{\boldsymbol{\mathcal{b}}}^{\mathrm{a}}_{s_i})_{k \neq k_m} \right\|_2 \tag{13}$$

where $\mathcal{F}(\boldsymbol{\mathcal{b}}_{s_i})_{k \neq k_m} \in \mathbb{C}^{N_s - 2M}$ refers to the DFT of $\boldsymbol{\mathcal{b}}_{s_i}$ where the components at the discrete frequencies k_m and $N_s - k_m$ are omitted. This ensures that the DFT of the actuation field sequence estimate $\mathcal{F}({}^{\mathbf{c}_i}\hat{\boldsymbol{\mathcal{b}}}^{\mathrm{a}}_{s_i})$ matches the DFT of the magnetic field measurement sequence $\mathcal{F}(\boldsymbol{\mathcal{b}}_{s_i})$ optimally for all discrete frequencies with the exception of k_m and $N_s - k_m$ (see Fig. 5b). A closed form solution for the coefficients $\mathbf{c}_i$ is derived in Appendix A. In the case illustrated in Fig. 5, the base sequences were chosen as $\boldsymbol{f}^{\mathrm{a}}_h[n] = n^{h-1}$ for $h \in \{1, 2, 3, 4\}$, where $\boldsymbol{f}^{\mathrm{a}}_h[n]$ refers to the n-th element of the sequence $\boldsymbol{f}^{\mathrm{a}}_h$. Note that this choice of base sequences corresponds to approximating the actuation field sequence $\boldsymbol{\mathcal{b}}^{\mathrm{a}}_{s_i}$ as a third order polynomial in time or sample index n. In general, a monomial base of H sequences corresponds to a polynomial approximation of order $H-1$ which can be interpreted as a Taylor approximation of order $H-1$. How well this approximation works generally depends on how big the higher order terms in the Taylor expansion of the field components $b^{\mathrm{a}}_{s_i}(t)$ are within the time interval of a measurement sequence. In general, a shorter measurement sequence duration T_{seq} and slower actuation field dynamics will lower the approximation error in the Taylor approximation. Slower actuation field dynamics (in the sense of decreased higher order derivatives of the actuation field), may be achieved by low pass filtering the desired actuation field. A higher approximation order H will also lower the approximation error but can lead to overfitting issues due to sensor noise. Which approximation order is appropriate for a given application typically has to be determined empirically by applying dynamic actuation fields on top of the localization fields in an experimental setup. The effect of different approximation methods and orders can then be determined in post-processing, which was also done in this work in the experimental section III-E. The actuation field compensation presented in this section helps in separating the DFT components originating from dynamic actuation fields from the DFT components caused by the localization field. In principle, the method could also be applied to separate the DFT contributions from other time-varying magnetic field sources, such as ferromagnetic continuum robots [18], from the localization field components.

4) Real time phasor field prediction: A prediction $\breve{\underline{\mathbf{b}}}_m(\mathbf{p}, \mathbf{i}^{\mathrm{a}})$ of the phasor fields in the workspace of the eMNS is required for pose estimation. The phasor fields generally depend on both the position and the actuation currents (under the assumption of constant localization current phasors). Different numerical and analytical methods exist for modelling $\underline{\mathbf{b}}_m(\mathbf{p}, \mathbf{i}^{\mathrm{a}})$. In this work, we adapt the Saturated Multipole Electromagnet Model (S-MPEM) from [1]. The phasor field at each frequency f_m is modelled as the product of a phasor field $\underline{\mathbf{b}}_m(\mathbf{p}, \mathbf{i}^{\mathrm{a}} = \mathbf{0})$ that is present when the actuation currents are zero and a scalar factor α_m that is used to model the saturation behaviour of the electromagnets in actuation current (see Fig. 2).

$$\underline{\mathbf{b}}_m(\mathbf{p}, \mathbf{i}^{\mathrm{a}}) \overset{\text{S-MPEM}}{\simeq} \alpha_m(\mathbf{i}^{\mathrm{a}}) \underline{\mathbf{b}}_m(\mathbf{p}, \mathbf{i}^{\mathrm{a}} = \mathbf{0}) \tag{14}$$

The model of the phasor field above leads to the following model for the phasor field prediction:

$$\breve{\underline{\mathbf{b}}}_m(\mathbf{p}, \mathbf{i}^{\mathrm{a}}) \overset{\text{S-MPEM}}{:=} \hat{\alpha}_m(\mathbf{i}^{\mathrm{a}}) \breve{\underline{\mathbf{b}}}_m(\mathbf{p}, \mathbf{i}^{\mathrm{a}} = \mathbf{0}) \tag{15}$$

The decoupling of $\breve{\underline{\mathbf{b}}}_m(\mathbf{p}, \mathbf{i}^{\mathrm{a}})$ into the factor $\hat{\alpha}_m(\mathbf{i}^{\mathrm{a}})$ and the field $\breve{\underline{\mathbf{b}}}_m(\mathbf{p}, \mathbf{i}^{\mathrm{a}} = \mathbf{0})$ allows us to obtain the phasor field prediction in two separate steps:

1) **Offline calibration of** $\breve{\underline{\mathbf{b}}}_m(\mathbf{p}, \mathbf{i}^{\mathrm{a}} = \mathbf{0})$: the workspace $\mathcal{W}$ is discretized (see Fig. 6), and the phasors $\underline{\mathbf{b}}_m(\mathbf{p}^{\mathrm{c}}, \mathbf{i}^{\mathrm{a}} = \mathbf{0})$ at each point $\mathbf{p}^{\mathrm{c}}$ of a calibration grid are measured in the absence of actuation currents. These measurements are then interpolated.
2) **Online estimation of** $\hat{\alpha}_m(\mathbf{i}^{\mathrm{a}})$: a reference sensor fixed to the coordinate system $\mathcal{K}_r$ measures the magnetic field during the navigation in the presence of actuation currents $\mathbf{i}^{\mathrm{a}}$ and is used to obtain the estimate $\hat{\alpha}_m(\mathbf{i}^{\mathrm{a}})$.

*a) **Offline calibration**:* this first step takes place offline prior to navigation and without actuation currents. A calibration sensor is attached to a positioning stage in a known orientation relative to $\mathcal{K}_0$. The sensor is moved to a calibration point $\mathbf{p}^{\mathrm{c}}$ belonging to a regular grid defined to sample the workspace (blue points in Fig. 6). The desired currents are set according to (2) with $i^{\mathrm{a}}_m(t) = 0$. The magnetic field is measured and an estimate $\hat{\underline{\mathbf{b}}}_m(\mathbf{p}^{\mathrm{c}}, \mathbf{i}^{\mathrm{a}} = \mathbf{0})$ is computed using (9). This step is repeated for all calibration points of the grid. The obtained phasor measurements are given in the coordinate frame $\mathcal{K}^c_s$ of the sensor during calibration. The orientation of $\mathcal{K}^c_s$ relative to $\mathcal{K}_0$ is known such that ultimately the phasors matrix can be expressed in $\mathcal{K}_0$. The value of the phasors at any position between the calibration points is interpolated using an interpolation method such as tricubic interpolation. Additionally, a reference sensor with reference sensor frame $\mathcal{K}_r$, placed near the electromagnets, measures the magnitudes $|\hat{\underline{\mathbf{b}}}^{r}_m|_{\mathbf{i}^{\mathrm{a}}=0}$ of the field phasors at the reference sensor position in the absence of any actuation currents.

*b) **Online estimation**:* this second step is performed online during navigation. The reference sensor measures the magnitude of the field phasors at its position $|\hat{\underline{\mathbf{b}}}^{r}_m|$ when actuation currents are generated. The factors α_m are then estimated as

$$\hat{\alpha}_m = \frac{|\hat{\underline{\mathbf{b}}}^{r}_m|}{|\hat{\underline{\mathbf{b}}}^{r}_m|_{\mathbf{i}^{\mathrm{a}}=0}} \tag{16}$$

and capture the influence of the actuation currents on the localization field.

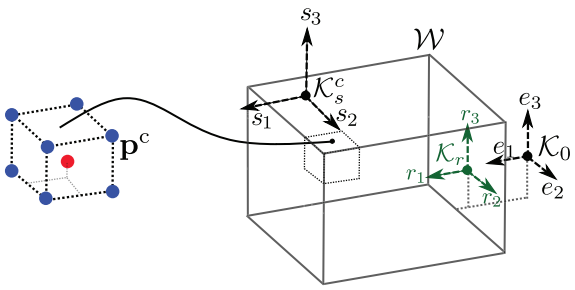

Fig. 6. Workspace $\mathcal{W}$ and coordinate system $\mathcal{K}_0$ of the eMNS. Calibration cells used to compute the phasor fields are indicated with dotted lines and bounded by the grid point vertices $\mathbf{p}^c$ in blue. A test point for evaluating the position estimate accuracy located in between the grid points is shown in red. The moving sensor with attached frame $\mathcal{K}_s^c$ is used to sample the magnetic fields. The position of the reference sensor coordinate system $\mathcal{K}_r$ outside the workspace is indicated.

5) Phasor vector magnitude prediction: For the estimation of the sensor position, a prediction of the phasor magnitude field $|\breve{\underline{\mathbf{b}}}_m|(\mathbf{p}, \mathbf{i}^a)$ in the workspace needs to be computed. In principle, this could be achieved by computing $|\breve{\underline{\mathbf{b}}}_m|(\mathbf{p}, \mathbf{i}^a) := |\breve{\underline{\mathbf{b}}}_m(\mathbf{p}, \mathbf{i}^a)|$ (e.g. first interpolate the phasor vector from the calibration grid measurements and then take the magnitude of that vector). However, this computation method is sensitive to errors caused by time delays in the phasor measurements (see also Fig. 4). Such errors can be avoided in the computation of $|\breve{\underline{\mathbf{b}}}_m|(\mathbf{p}, \mathbf{i}^a)$ by first computing the magnitude of the phasor vectors on the calibration grid points $|\hat{\underline{\mathbf{b}}}_m(\mathbf{p}^c, \mathbf{i}^a = \mathbf{0})|$ (this computation is not affected by errors caused by sensor acquisition delays) and then interpolating these phasor magnitude values.

D. Pose estimation

1) Position: First, the position of the sensor is estimated regardless of its orientation. Given the prediction for the phasor magnitude field $|\breve{\underline{\mathbf{b}}}_m|(\mathbf{p}, \mathbf{i}^a)$ and the estimated phasors at the location of the sensor, an estimate $\hat{\mathbf{p}}$ of the location of the magnetic sensor is obtained by minimizing a quadratic objective function as follows:

$$\hat{\mathbf{p}} = \underset{\mathbf{p}}{\operatorname{argmin}} \sum_m \left(|\hat{\underline{\mathbf{b}}}_m| - |\breve{\underline{\mathbf{b}}}_m|(\mathbf{p}, \mathbf{i}^a) \right)^2 \tag{17}$$

where $|\hat{\underline{\mathbf{b}}}_m|$ refers to the magnitude of the estimated phasor vectors at the location of the sensor as defined in (10).

2) Orientation: We then estimate the orientation of the coordinate system $\mathcal{K}_s$ aligned with the axes of the sensor (see Fig. 1b) with respect to the coordinates system $\mathcal{K}_0$ fixed to the eMNS and in which the phasors map is known (see Fig. 1a). The relationship between the phasors expressed in $\mathcal{K}_s$ and $\mathcal{K}_0$ is given by

$$\mathbf{R}[\underline{\mathbf{b}}_m]_{\mathcal{K}_s} = [\underline{\mathbf{b}}_m]_{\mathcal{K}_0} \tag{18}$$

with $\mathbf{R}$ the rotation matrix from $\mathcal{K}_s$ to $\mathcal{K}_0$. Given the position estimate $\hat{\mathbf{p}}$ from (17) and the prediction for the phasor field from (15), we can predict the phasors present at the position of the sensor as $[\breve{\underline{\mathbf{b}}}_m(\hat{\mathbf{p}}, \mathbf{i}^a)]_{\mathcal{K}_0}$. Given the phasor measurements from the sensor, we compute an estimate $\hat{\mathbf{R}}$ of the rotation matrix which minimizes the following objective function for $\mathbf{R} \in SO(3)$

$$\left\| \mathbf{R}[\hat{\underline{\mathbf{b}}}_m]_{\mathcal{K}_s} \mathbf{W} - [\breve{\underline{\mathbf{b}}}_m(\hat{\mathbf{p}}, \mathbf{i}^a)]_{\mathcal{K}_0} \right\|_F \tag{19}$$

with $\mathbf{W} = \operatorname{diag}(w_1, \cdots, w_M)$ a diagonal matrix which multiplies each measurement phasor with a complex valued weight w_m. Introducing this weighting matrix allows for the compensation of phase shifts due to measurement delays (see Fig. 4d) and errors on the estimated phasor magnitude due to noise. Finding both an estimate $\hat{\mathbf{W}}$ of the weighting matrix and $\hat{\mathbf{R}}$ of the rotation matrix to minimize (19) is known as a weighted orthogonal Procrustes problem. A numerical algorithm for solving this problem for real matrices is found in [23], and can be extended to complex matrices, which results in Algorithm 1. It solves the problem by applying two solution steps iteratively. In the first step, (19) is minimized for the rotation matrix where the weights are considered constant. This problem is a regular orthogonal Procrustes problem with complex matrices whose solution is derived in Appendix B-A. In a second step, the optimal weights that further minimize (19) for the given rotation matrix estimated during the first step are computed. The solution for the optimal weights is derived in Appendix B-B. At each new iteration, the first step is applied using the updated weight estimates, and the procedure is repeated until convergence on the weight values occurs.

Algorithm 1 Orientation estimation procedure

Input
$\mathbf{A} := [\hat{\underline{\mathbf{b}}}_m]_{\mathcal{K}_s} \in \mathbb{C}^{3\times M}$ ▷ Phasor measurement matrix
$\mathbf{B} := [\breve{\underline{\mathbf{b}}}_m(\hat{\mathbf{p}}, \mathbf{i}^a)]_{\mathcal{K}_0} \in \mathbb{C}^{3\times M}$ ▷ Estimated phasor matrix
Output
$\hat{\mathbf{R}} \in SO(3)$ ▷ Estimate for rotation
$\hat{\mathbf{W}} = \operatorname{diag}(w_1, \cdots, w_M) \in \mathbb{C}^{M\times M}$ ▷ Estimate for weights

$\hat{\mathbf{W}} \leftarrow \mathbf{I}_3$ ▷ Initialize weights
$\delta \leftarrow \infty$ ▷ Initialize convergence criterion
while $\delta > \epsilon$ **do**
Step 1: Estimate $\hat{\mathbf{R}}$ given $\hat{\mathbf{W}}$
$\mathbf{U}, \mathbf{\Sigma}, \mathbf{V} \leftarrow \text{SVD}(\text{Re}\{(\mathbf{A}\hat{\mathbf{W}})\mathbf{B}^H\})$ ▷ Compute SVD
$\hat{\mathbf{R}} \leftarrow \mathbf{V}\operatorname{diag}(1, \cdots, \det(\mathbf{U}\mathbf{V}^T))\mathbf{U}^T$ ▷ Update $\hat{\mathbf{R}}$
Step 2 : Estimate $\hat{\mathbf{W}}$ given $\hat{\mathbf{R}}$
$\mathbf{X} \leftarrow \mathbf{A}^H\mathbf{A}$ ▷ $\mathbf{X} \in \mathbb{R}^{M\times M}$
$\mathbf{Y} \leftarrow \mathbf{B}^H\hat{\mathbf{R}}\mathbf{A}$ ▷ $\mathbf{Y} \in \mathbb{C}^{M\times M}$
$w_i' \leftarrow \mathbf{Y}[i,i]^*/\mathbf{X}[i,i]$ ▷ Compute weights
$\hat{\mathbf{W}} \leftarrow \operatorname{diag}(w_1', \cdots, w_M')$ ▷ Update $\hat{\mathbf{W}}$
Check convergence
$\delta \leftarrow \max(|w_i - w_i'|/|w_i|)$ ▷ Compute δ
$w_i \leftarrow w_i'$ ▷ Update weights
end while

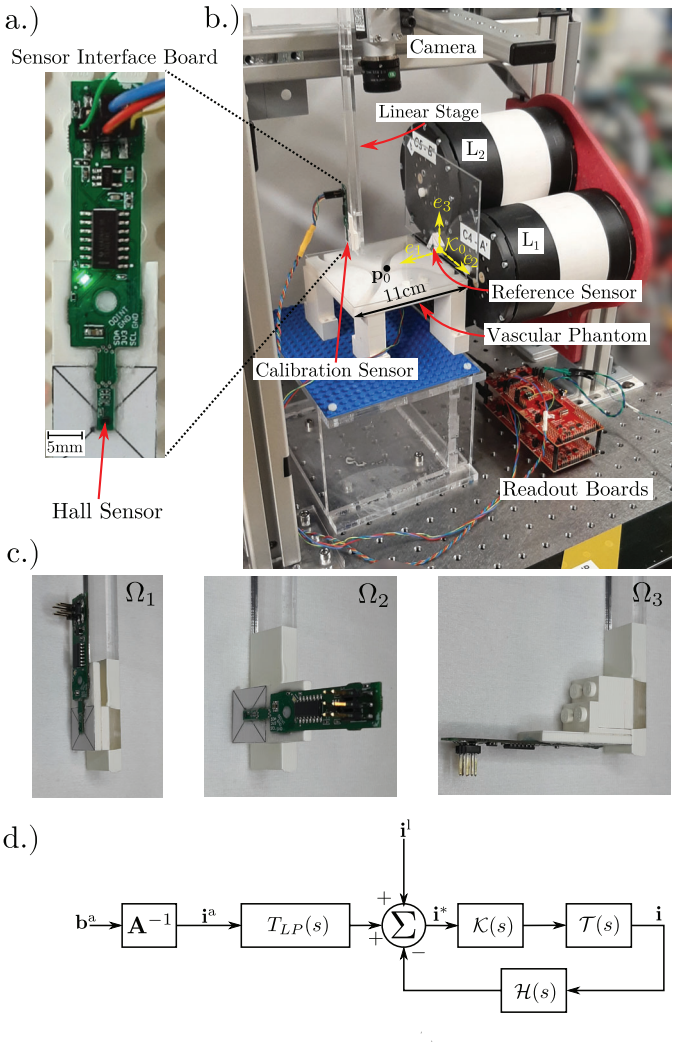

Fig. 7. Experimental setup. a) Interface board for the three-axis Hall sensor. b) Overview of the experimental platform. c) Calibration sensor mounted in different orientations $\{\Omega_1, \Omega_2, \Omega_3\}$ on the effector of the linear stage. d) Control loop used to generate actuation and localization fields.

III. Results

A. Experimental setup

Our method is evaluated experimentally using the eMNS consisting of the three cylindrical electromagnets depicted in Fig. 7b. The currents in the electromagnets are driven using a custom power amplifier supplied by two laboratory power supplies that provide a voltage of $90\,\mathrm{V}$ and a power of $450\,\mathrm{W}$ to the amplifier. The currents were controlled using the control loop depicted in Fig. 7d that was implemented on a TMDSCNCD28388D control card from Texas Instruments. The actuation currents were computed using a linear model of the eMNS:

$$\mathbf{i}^{\mathrm{a}} = \mathbf{A}^{-1}\mathbf{b}^{\mathrm{a}}(\mathbf{p}_0) \tag{20}$$

with $\mathbf{A}$ an actuation matrix identified experimentally using the calibration procedure proposed in [22] at the position $\mathbf{p}_0$ at the center of the workspace defined as

$$\mathcal{W} = [20, 100] \times [-40, 40] \times [-30, 30]\ \mathrm{mm}$$

in coordinates of $\mathcal{K}_0$ that is attached to the center of the eMNS front surface in Fig. 7b. The reference sensor is attached to the front surface of the coils as shown in Fig. 7b. The desired actuation currents were low-pass filtered with a cutoff frequency of $10\,\mathrm{Hz}$ (filter denoted T_{LP} in Fig. 7d). A PI controller $\mathcal{K}(s)$ was used to track the desired currents. The measurements from the current sensors were filtered using an anti-aliasing filter $\mathcal{H}(s)$. The actuation currents were controlled using a ROS (Robot Operating System) based software framework that overlaid the images of the camera in real-time with an actuation field map. The amplitude of the oscillating currents was chosen as $400\,\mathrm{mA}$, which resulted in a mean oscillation amplitude of the magnetic field of $630\,\mu\mathrm{T}$ throughout the workspace. The localization current amplitude and oscillation frequencies were chosen to ensure that the catheter model used in section III-F did not show noticeable vibrations even when held close to the coils and that such vibrations would remain significantly smaller than the precision resulting from the localization method as mentioned in section II-B. The voltage amplitudes necessary to generate these oscillating currents were in the range of $15\,\mathrm{V}$ to $22\,\mathrm{V}$.

For the calibration of the phasor fields, the workspace was discretized as a regular grid with a grid spacing of $2\,\mathrm{cm}$ (see one calibration cell delimited by the blue points in Fig. 6). Tricubic interpolation from the Python Scipy package was used for the interpolation of the phasor magnitude fields and trilinear interpolation was used for the interpolation of the phasor fields. The magnetic measurements were performed with a three-axis Hall sensor AKM09973D (Fig. 7a) that exhibits a measurement range of $36\,\mathrm{mT}$ and a resolution of 16 bits for all three sensor directions. Measurements were acquired in low-noise mode at $500\,\mathrm{Hz}$. The gains of the sensor were measured and compensated for using a Helmholtz coil in order to minimize errors due to sensitivity mismatches between different sensor Hall elements. Synchronization between magnetic field measurements and localization field generation was obtained by sending a synchronization signal from the driver to the readout boards connected to the Hall sensor interface boards at the start of each localization period. The implementation ensured that the measurement delay ΔT remained below 1 ms (see II-C2 and Fig. 4).

The ground-truth for the pose during the calibration and for the estimation of the precision and accuracy of the localization was obtained by mounting the sensor on a three-axis linear position stage from SmarAct. Both the electromagnets and the measurement setup, consisting of linear stage and sensor mounted on a plastic rod, had to be dismounted in between different sets of experiments. In order to avoid absolute orientation and position errors caused by remounting the sensor and positioning stage, a calibration was obtained prior to conducting the set of experiments. The experimental conditions in the remainder of this section are summarized in Table I.

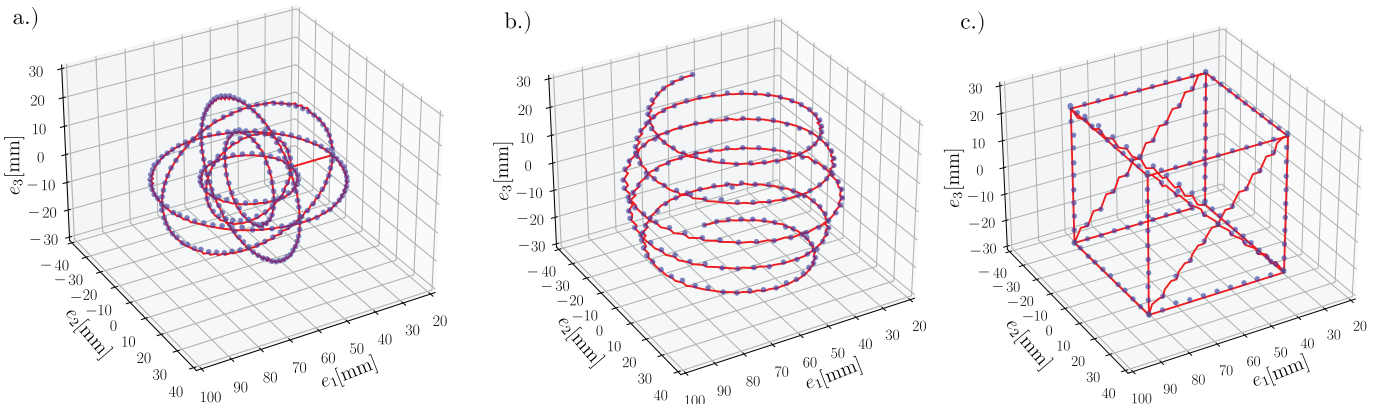

Fig. 8. Localization method applied to test sets T4 to T6 (without actuation field). The trajectory of the linear stage is indicated in red and the position estimates in blue. a) T4: circles trajectory. b) T5: spiral trajectory. c) T6: cube trajectory

TABLE I
EXPERIMENTAL CONDITIONS.

Experiment	$(f_1$	f_2	$f_3)$ [Hz]	f_{seq} [Hz]	Actuation field
III-B	(92	98	104)	2	No
III-C	(92	98	104)	2	Yes (static)
III-D1	(92	98	104)	2	No
III-D2	(70	90	110)	2, 5, 10	No
III-E	(70	90	110)	10	Yes (dynamic)
III-F	(70	90	110)	10	Yes (dynamic)

TABLE II
POSE ESTIMATE ERROR WITHOUT ACTUATION FIELD.

Test set				Localization accuracy	
	Positions	Orientation	N	$\overline{e_{\mathbf{p}}}$ [mm]	$\overline{e_{\mathbf{R}}}$ [°]
T1	Grid	Ω_1	48	0.27	0.48
T2	Grid	Ω_2	48	0.36	1.83
T3	Grid	Ω_3	48	0.36	1.73
T4	Circles	Ω_1	296	0.38	0.61
T5	Spiral	Ω_1	201	0.32	0.56
T6	Cube	Ω_1	176	0.58	0.59

B. Accuracy of the pose estimation

We first evaluated the pose estimation method in the absence of an actuation field. The Hall sensor was attached to the linear position stage in different reference orientations (see Fig. 7b and c). The stage was used to drive the sensors at different poses divided into six different test sets, T1 to T6. The sets T1 to T3 were composed of grid points located between the calibration points (indicated in red in Fig. 6), and the sensor was oriented in three different orientations (Ω_1, Ω_2 and Ω_3 depicted in Fig. 7c). The sets T4 to T6 were composed from positions sampled over three different types of trajectories (see Fig. 8) and with the sensor in orientation Ω_1. For each test set, N poses were evaluated (see Table II) and their pose estimates were averaged out over 16 measurement sequences in order to reduce noise.

1) Position: Measurements are collected at each position with the linear stage providing the ground truth position $\mathbf{p}_n$ with $n \in \{1, \dots, N\}$. The position at each test point was estimated using (17) resulting in the mean positional estimate $\hat{\mathbf{p}}_n$. The error in the position estimation of the n-th test point is evaluated using the Euclidean distance between the ground-truth and position estimate $e_{\mathbf{p}} = \|\mathbf{p}_n - \hat{\mathbf{p}}_n\|_2$. The mean position estimation error over the whole test set is then obtained as $\overline{e_{\mathbf{p}}} = \frac{1}{N}\sum_n e_{\mathbf{p}}$.

The mean position estimate errors for the different test sets and the different sensor orientations are listed in Table II, and Fig. 8 shows the position estimates compared to the ground truth trajectories for the test sets T4 to T6. The mean error was slightly higher for the orientations Ω_2 and Ω_3, which was attributed to an imperfect calibration of the sensor gains and did not affect the measurements in orientation Ω_1, since this orientation was the same as during the calibration.

2) Orientation: The mean rotation matrix $\hat{\mathbf{R}}_n$ with $n \in \{1, \dots, N\}$ for each test point was estimated using Algorithm 1. The accuracy of the orientation estimate at the n-th test position is evaluated using the following error metric:

$$e_{\mathbf{R}} = \left\| \log\left(\hat{\mathbf{R}}_n^T \mathbf{R}^{\text{ref}} \right) \right\|_2 \tag{21}$$

with $\mathbf{R}^{\text{ref}}$ the expected rotation matrix of the sensor for its orientation $\Omega \in \{\Omega_1, \Omega_2, \Omega_3\}$ during each test set. This metric represents the angle of the smallest rotation necessary to align the rotation matrices $\hat{\mathbf{R}}_n$ and $\mathbf{R}^{\text{ref}}$ [24]. The mean orientation estimation error over the whole test set is then obtained as $\overline{e_{\mathbf{R}}} = \frac{1}{N}\sum_n e_{\mathbf{R}}$. Table II lists the mean orientation error for the different test sets. The orientation errors for test sets with orientations Ω_2 and Ω_3 were again higher than Ω_1. In addition to the aforementioned imperfect sensor calibration, the orientation accuracy could also be affected by an inaccurate rotation of the sensors in Fig. 7c.

C. Influence of the static actuation field on the pose estimation

As outlined in section II-C4, the phasor fields depend on the actuation currents. Although this effect is captured by the

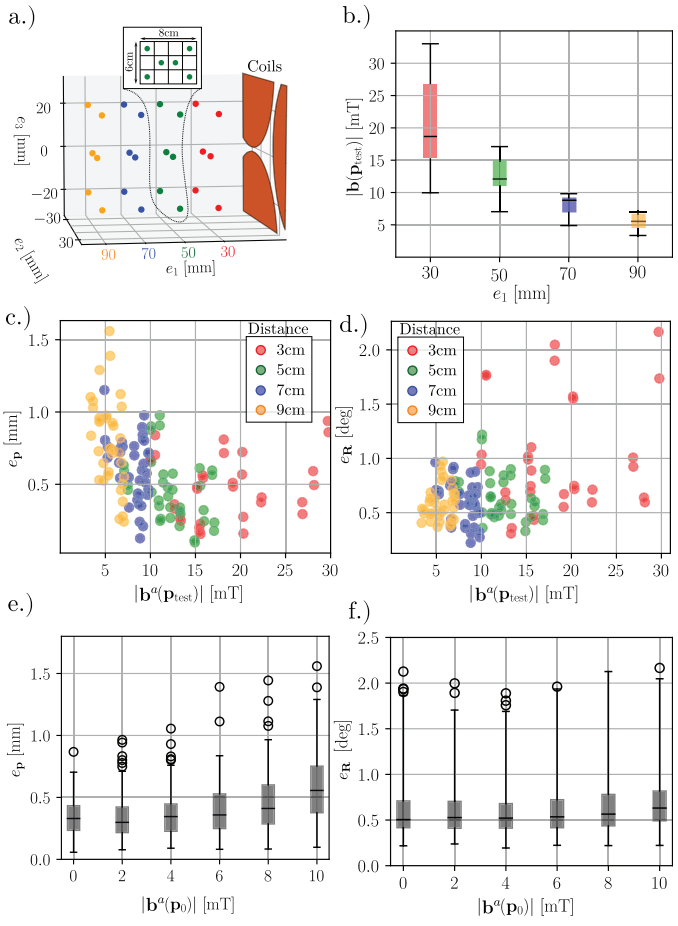

Fig. 9. Influence of static actuation fields on the pose estimation. a) Test points located in between calibration grid points. b) Actuation field magnitude distributions at every test point $\mathbf{p}_{\text{test}}$ over their distance from the electromagnets for $|\mathbf{b}^{\text{a}}(\mathbf{p}_0)| = 10$ mT generated along $\mathbf{e}_1$. Position c) and orientation d) estimate errors at the test positions for six different field orientations and $|\mathbf{b}^{\text{a}}(\mathbf{p}_0)| = 10$ mT. Position e) and orientation f) error distributions over the magnitude of the actuation field at $\mathbf{p}_0$.

phasor field estimate (15), it does not perfectly compensate for the nonlinear behaviour of the eMNS, and the generation of actuation fields is thus expected to affect the accuracy of the pose estimation. In order to evaluate this effect experimentally, the pose of the sensor was estimated while generating static actuation fields with the eMNS.

The test points for this experiment are depicted in Fig 9a and consist of a subset of the test points used in T1-3 at distances $\{30, 50, 70, 90\}$ cm from the coils (the distance is indicated by the color scheme). A set of actuation fields was generated using (20) for combinations of different directions and magnitudes so that $\mathbf{b}^{\text{a}}(\mathbf{p}_0) = b\,\mathbf{e}$, with $\mathbf{e} \in \{\mathbf{e}_1, \mathbf{e}_2, \mathbf{e}_3, -\mathbf{e}_1, -\mathbf{e}_2, -\mathbf{e}_3\}$, and $b \in \{0, 2, 4, 6, 8, 10\}$ mT. The actuation field magnitude measured at the test points for $b = 10\,\text{mT}$ and $\mathbf{e} = \mathbf{e}_1$ are depicted in Fig. 9b as a function of the distance of each test point from the coils' surface. The position and orientation estimate accuracies for each test position and for each applied actuation field were evaluated as in section III-B using the same error metrics. Figures 9c and d show the position and orientation errors for $b = 10\,\text{mT}$, and Fig. 9e and f the distribution of position and orientation

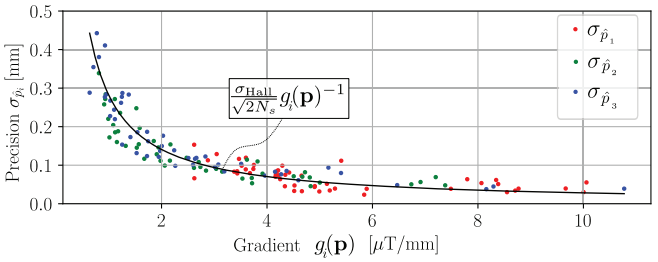

Fig. 10. Precision of the position estimate over the gradient $g_i(\mathbf{p})$ defined in (23) for $T_{\text{seq}} = 500\,\text{ms}$, with $\sigma_{\hat{p}_i}$ the standard deviation on the position estimate component $\hat{p}_i$. Precisions predicted using (22) are indicated using the black line.

estimate errors as a function of b.

Different effects lead to systematic errors in the pose estimation. The prediction of the phasor fields is not ideal and subject to inaccuracies in the magnetic field model (15), such as interpolation errors, which increase closer to the electromagnets due to the higher curvature of the magnetic field components in this region. The measurements of the phasors are also subject to systematic errors due to differences in the Hall element sensitivities despite careful calibration. The sensitivity of the position estimation to such systematic errors in the phasor measurements increases with distance from the coils. In Fig. 9c, the position estimation error increases with distance from the coils which may be explained by the fact that the position estimation procedure becomes more sensitive to relative errors in the phasor estimation and prediction. Closer to the coils, the error increases again slightly which may be due to increased errors in the phasor magnitude field prediction as a result of interpolation or other modelling errors that increase closer to the coils. The orientation estimation in Fig. 9d increases closer to the coils which is likely due to increased phasor field prediction errors, presumably interpolation errors, that lead to a less accurate prediction of the phasor vector directions. This conclusion is supported by the fact that in 9f, the orientation error does not increase significantly with applied actuation field. This indicates interpolation errors in the field prediction 15, that do not increase with actuation field, are the dominant source of errors for the orientation estimate. The position estimation error increased from a mean of 0.35 mm to around 0.6 mm with applied actuation field (Fig. 9e) which indicates that the actuation field is the main contributor to position estimate errors.

D. Precision of the pose estimation

1) Influence of the magnetic field gradient: Measurements are subject to both intrinsic noise from the sensor and noise generated by the eMNS. Consider the position $\mathbf{p} = \begin{bmatrix} p_1 & p_2 & p_3 \end{bmatrix}^T_{\mathcal{K}_0}$ and its estimate $\hat{\mathbf{p}} = \begin{bmatrix} \hat{p}_1 & \hat{p}_2 & \hat{p}_3 \end{bmatrix}^T_{\mathcal{K}_0}$, it is shown in Appendix C that the precision of the localization estimate $\sigma_{\hat{p}_i}$ of the given method is given by:

$$\sigma_{\hat{p}_i}(\mathbf{p}) = \frac{\sigma_{\text{Hall}}}{\sqrt{2N_s}} \cdot g_i(\mathbf{p})^{-1} \tag{22}$$

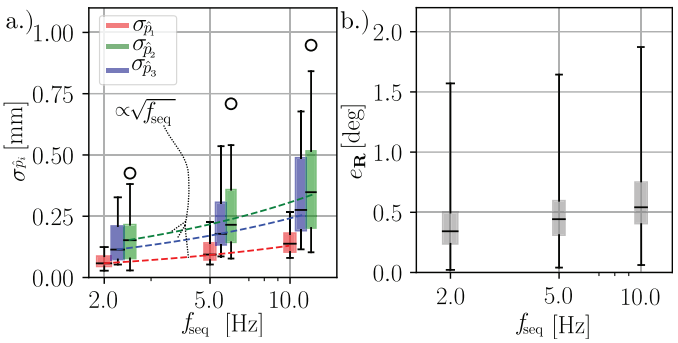

Fig. 11. Precision of the pose estimate over the localization frequency f_{seq}. a.) Standard deviations on the position estimate components. b) Orientation error distributions.

In this equation σ_{Hall} refers to the RMS noise of the Hall sensor (which is assumed to be equal for all three measurement directions), N_s is the number of samples in the measurement sequence and the gradient g_i is defined as

$$g_i(\mathbf{p}) = \left(\sqrt{\sum_m \left(\frac{\partial |\underline{\mathbf{b}}_m|}{\partial p_i} \Big|_{\mathbf{p}} \right)^{-2}} \right)^{-1} \tag{23}$$

In Fig. 10, the standard deviations $\sigma_{\hat{p}_i}$ of the positional estimates in e_1- e_2- and e_3-direction are plotted against the gradient $g_i(\mathbf{p})$ introduced in (23). The precision of the positional estimates was evaluated by computing the standard deviation $\sigma_{\hat{p}_i}$ of 16 estimated position coordinates at each test point. The gradients were computed from the calibration introduced in II-C4 by computing the spatial difference quotients of the field magnitudes and interpolating the obtained values using tricubic interpolation. The precision in e_1-direction, pointing away from the coils, was generally the best due to higher magnetic field gradients in this direction. The localization precision in e_2- and e_3-direction showed similar values and were worse than those in the e_1-direction.

2) Influence of the localization frequency: We evaluated the influence of the measurement sequence duration on the precision of the localization for f_{seq} equal to 2 Hz, 5 Hz and 10 Hz. Figure 11a shows the measured standard deviations of the positional estimates in e_1-, e_2-, and e_3-direction as a function of f_{seq}. The standard deviations of the position estimate components showed an increase approximately proportional to $\sqrt{f_{\text{seq}}}$ as indicated by the dashed lines. Figure 11b shows the distribution of the orientation errors for all test points in the workspace in dependence of f_{seq}.

E. Influence of dynamic actuation field on the pose estimation

The generation of transient actuation fields introduces errors in the pose estimation (see section II-C3). To reduce this effect, the actuation field is compensated for in the measurements using (10). Here, we evaluate this compensation method experimentally. The pose of a sensor located at the center of the workspace was estimated while simultaneously applying a set of sinusoidally oscillating actuation fields at a magnitude of 10 mT and direction e_1. The actuation field

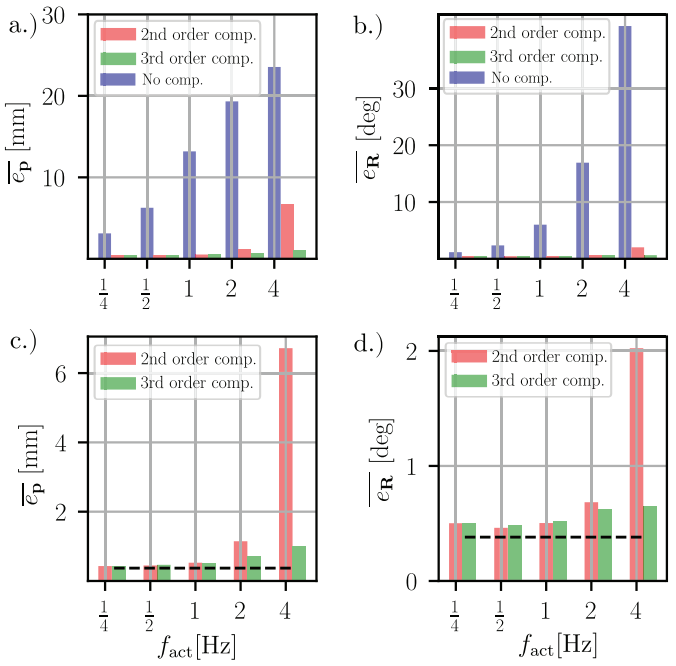

Fig. 12. Influence of dynamic actuation fields on the pose estimation with and without compensation for a 10 mT sinusoidal actuation field in e_1 direction oscillating at different frequencies f_{act}. a) Mean position and b) mean orientation estimate error. Close-ups for 2nd and 3rd order for the compensation in c) and d). The mean error for the zero applied actuation field is indicated by the dotted black line.

frequencies were chosen as $f_{\text{act}} \in \{0.25, 0.5, 1, 2, 4\}$ Hz. The base sequences used to estimate the actuation field within a sequence according to (12) were chosen as either 2nd degree polynomials ($H = 3$) or 3rd degree polynomials ($H = 4$), and (13) was used to compute the value of the coefficients $c_{i,h}$:

$$\hat{\boldsymbol{\beta}}^{\text{a}}_{s_i}[n] = \sum_{h=1}^{H} c_{i,h} n^{h-1} \tag{24}$$

Figure 12 shows the evolution of the pose estimation error as a function of applied actuation frequency with and without compensation of the actuation field. The compensation significantly reduces errors caused by transient actuation fields. The 2nd and 3rd degree compensation offer a similar performance up to an actuation frequency of 1 Hz. At 2 and 4 Hz, the approximation of the actuation field is worse for the 2nd degree polynomial compared to the 3rd degree polynomial, leading to increased errors in the pose estimation.

F. Simultaneous actuation and pose estimation of a catheter

In order to demonstrate simultaneous actuation and localization in a realistic case, a catheter model was fabricated as depicted in Fig. 13a. Its rigid tip embeds an AKM09973D 3-axis Hall effect sensor and an NdFeB cylindrical magnet of 3 mm in diameter and 6 mm in length. The sensor was placed approximately 6 mm from the permanent magnet in order to avoid saturation of the sensor. Under these conditions, the permanent magnet generated a field of around 10 mT in the s_2 direction of the sensor. Since the sensor has a range of 35 mT, actuation fields of up to 25 mT can be generated

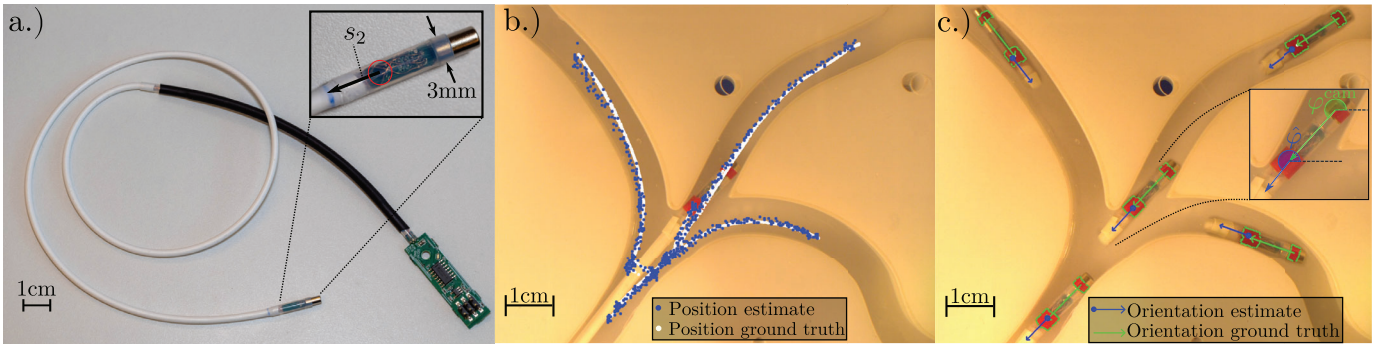

Fig. 13. Simultaneous actuation and localization of a magnetic catheter in a flat vascular model. a) Design of the magnetic catheter with a tip-integrated Hall sensor (red circle) and distal magnet. b) position estimate in phantom plane and c) orientation estimate compared to the ground-truth projected in the camera view for the different poses of the tip over the trajectory.

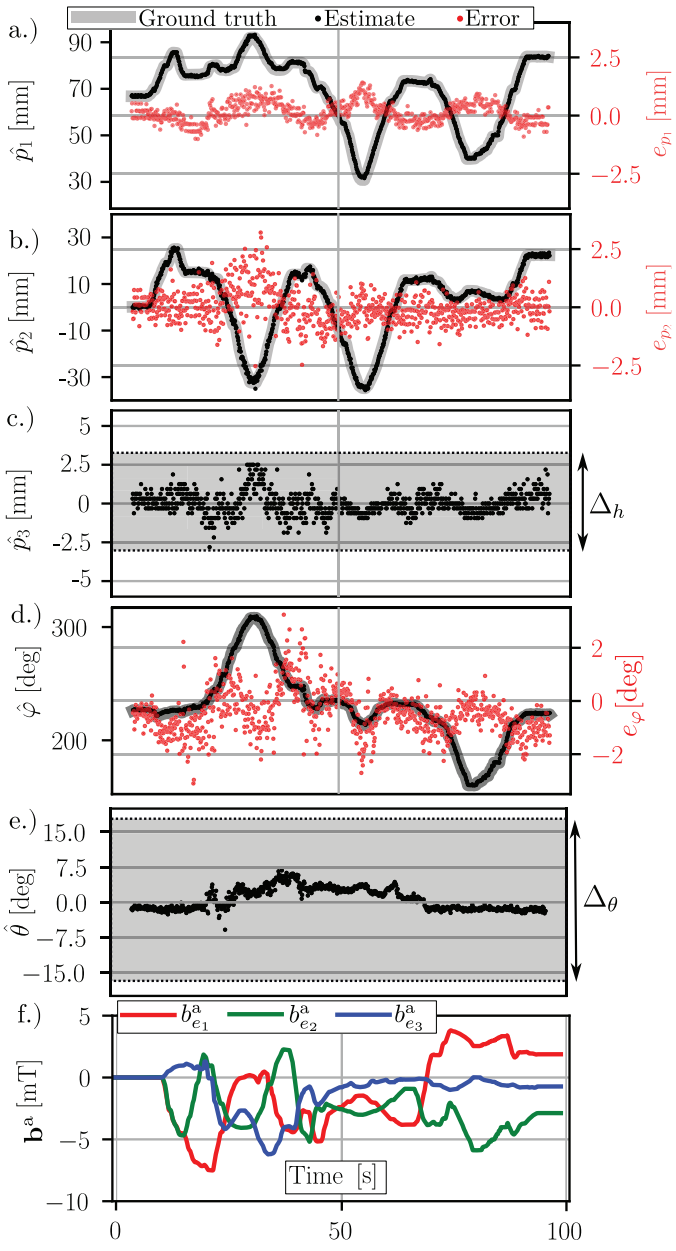

Fig. 14. Experimental data for simultaneous actuation and localization of a magnetic catheter in a flat vascular model. a)-e) Pose estimate. f) Actuation field measured by the Hall sensor.

without saturating the sensor. The catheter was steered through a flat vascular phantom (see Fig. 13b) by applying actuation fields in different directions (see Fig. 14f) and simultaneously advancing or retracting the catheter with a manually operated catheter advancement mechanism[1]. In addition to demonstrating simultaneous actuation and localization of a tethered object, the purpose of this experiment is to evaluate how possible motion of the catheter caused by the localization field affects the pose estimation.

The ground-truth for the 2d-position and orientation of the catheter's rigid tip in the plane of the phantom was provided by an overhead camera Basler acA1920-40gc (see Fig. 7b), which tracked two red markers placed on the tip and at known locations with respect to the sensor (see Fig. 13c). The vascular phantom and camera were placed at a known calibrated pose in front of the eMNS, so that the camera provides the ground-truth 2d-position $\mathbf{p}^{\text{cam}} = \begin{bmatrix} p_1^{\text{cam}} & p_2^{\text{cam}} \end{bmatrix}^T$ along the axes e_1 and e_2 in $\mathcal{K}_0$, and orientation φ^{cam} in the plane of the 2d phantom of normal direction e_3 (see Fig. 13c). The axis s_2 of the Hall sensor was aligned with the main axis of the catheter tip, so that the estimated angle $\hat{\varphi}$ could be retrieved from the rotation matrix estimate $\hat{\mathbf{R}}$. We also retrieved an estimate of the inclination angle denoted $\hat{\theta}$ corresponding to the angle formed between the main axis of the catheter tip and the plane of the vascular model. For the localization fields, the frequencies $f_m \in \{70, 90, 110\}$ Hz were chosen. For the given localization currents, a camera position estimation noise of $\sigma_{p_1}^{\text{cam}} = \sigma_{p_2}^{\text{cam}} = 27\ \mu m_{rms}$ was measured when the localization field was applied to the catheter in the center of the workspace. From these measurements, it can be concluded that the catheter motion resulting from the localization field is an order of magnitude smaller than the localization precision measured in Section III-D.

The ground-truth measurements were linearly interpolated over time for comparison with the pose estimates. The accuracy of the 2d-position estimate can be evaluated using the Euclidean distance

$$e_{\mathbf{p}} = \sqrt{e_{p_1}^2 + e_{p_2}^2} \tag{25}$$

[1]A video of this experiment is available as a multimedia attachment with this paper.

with $e_{p_i} = p_i^{\text{cam}} - \hat{p}_i$ the relative error on each component of the 2d-position. The accuracy of the orientation estimate can be evaluated based on the relative difference in the angle

$$e_\varphi = \varphi^{\text{cam}} - \hat{\varphi} \tag{26}$$

The mean position error along the trajectory was evaluated at $\overline{e_{\mathbf{p}}} = 0.68\,\text{mm}$ and the mean absolute angle error $\overline{|e_\varphi|}$ at $0.79°$ where the averaging was done over time from the beginning to the end of the catheter motion. Figure 14a-e shows the evolution of the pose estimates over time. Although no ground-truth exists for the component p_3 and θ, their estimate $\hat{p}_3$ and $\hat{\theta}$ stayed within the range imposed by the geometry of the 2d phantom depicted by the gray zones in Fig. 14c and e. The values Δ_h and Δ_θ are the maximum range of vertical motion and inclination angle that we estimated considering the dimension of the vascular model and the rigid catheter tip. The estimation errors for the observed degrees of freedom $\{\hat{p}_1, \hat{p}_2, \hat{\varphi}\}$ stayed in the expected range of errors determined from the experiments with the 3D positioning stage in sections III-C and III-E. From this, it can be concluded that possible errors due to catheter motion caused by the localization field do not lead to a notable increase in overall pose estimation errors.

G. Scaling considerations

Both the precision of the localization method, and the necessary electrical requirements of the driver to generate the localization field are affected by the dimension of the eMNS and of its workspace. Consider a system that is scaled up by a factor $\gamma > 1$ in linear dimension compared to the one used in this paper. We assume such a system would generate the phasor fields $\underline{\mathbf{b}}'_m(\mathbf{p})$ given by:

$$\underline{\mathbf{b}}'_m(\mathbf{p}) = \underline{\mathbf{b}}_m(\mathbf{p}/\gamma) \tag{27}$$

E.g. the amplitudes of the localization fields are the same but extend over the scaled workspace.

1) Precision: The general expression for the precision $\sigma_{\hat{p}_i}(\mathbf{p})$ given in (22) is proportional to the inverse gradient $g_i(\mathbf{p})^{-1}$ given in (23). The localization precision $\sigma'_{\hat{p}_i}$ of the scaled system becomes

$$\sigma'_{\hat{p}_i}(\gamma\mathbf{p}) = \gamma\sigma_{\hat{p}_i}(\mathbf{p}) \tag{28}$$

which follows directly from (23). Therefore, the precision is expected to scale linearly with the system size.

2) Active and reactive power: The generation of the localization field requires the transmission of reactive power to the electromagnets. In order to do this, an oscillatory voltage needs to be applied to the electromagnet on top of the voltage required for actuation. For the system considered in this work, around 36 V was needed to drive the maximum actuation current of 10 A and around 22 V was needed to drive the localization current of 0.4 A at the maximum frequency of 110 Hz. For a scaled electromagnet, driven with the same actuation current density, it can be shown that the active power to drive the maximum actuation current scales as $P \sim \gamma^3$ and the reactive power to drive the localization currents scales as $Q \sim \gamma^4$ given the assumptions on the magnitude of the localization field. The maximum actuation field would scale as $|\mathbf{b}^{\text{a}}_{\text{max}}| \sim \gamma$.

Consider a $\gamma := 2.5$ scaled system with a workspace $\mathcal{W}'$ of the following dimensions:

$$\mathcal{W}' = [50, 250] \times [-100, 100] \times [-75, 75]\ \text{mm}$$

which would be relevant for clinical applications. For such a system, the maximum power dissipated in the electromagnet P would increase from 360 W to 5.6 kW, and the maximum reactive power transfer to the electromagnet Q would increase from 220 VAr to 8.5 kVAr. Note that the required Q increases stronger since Q scales stronger than P. The power requirements could be implemented using a driver with current capacity of 35 A and output voltage of 450 V. The system would generate an increased maximum field of $|\mathbf{b}^{\text{a}}_{\text{max}}| = 25$ mT at the center of its workspace due to the actuation field scaling.

IV. Discussion & Conclusions

We propose a method to estimate the pose of a three-axis magnetic field sensor within the workspace of an eMNS, while simultaneously generating actuation fields to steer a magnetic device in which the sensor is to be embedded. The method can be used to simultaneously localize and actuate medical devices, which extends the functionality of an eMNS from pure actuation, to both actuation and localization, effectively making the eMNS a 2-in-1 system. To steer the device, this method only requires a magnetic sensor to be integrated into the device, thus favoring a miniaturization of the hardware necessary to implement this strategy. Our method is generic and can be applied to any eMNS composed of more than two electromagnets.

The method was demonstrated in a volume of $80 \times 80 \times 60$ mm using an eMNS composed of three electromagnets. In these conditions, the pose was estimated at a localization frequency of up to 10 Hz. We consistently showed a mean position accuracy and precision below 1 mm in our experiments, and a mean orientation error of less than 2° throughout the various tests we performed. Our method accounts for phase shifts in the measurements caused by time acquisition delays, thus eliminating the need for precise hardware-based synchronized acquisition between the calibration and online localization measurements.

To demonstrate how the localization and actuation of a medical device can work with the proposed method, a catheter prototype was constructed and steered through a flat phantom at a localization frequency of 10 Hz. Under these conditions and with actuation fields up to approximately 8 mT, the 2D mean position estimation error was measured as 0.68 mm and the planar angle error was measured as $0.79°$. A limitation of the demonstration catheter prototype was the rigid tip of 6 mm length. This limitation could be addressed in the future by making the link between the sensor and the distal magnet flexible. In order to account for rotations between the sensor and the distal magnet, the position of the distal magnet relative to the sensor could be estimated using DC measurements of the Hall sensor which are so far not used by the presented localization method. The localization method presented in this

paper lends itself for the localization of tethered surgical tools such as catheters, guidewires or endoscopes.

Due to the relatively low signal to noise ratio of the phasor measurements, the localization frequency was limited to 10 Hz to achieve a mean precision of approximately 0.35 mm throughout the workspace. For scaled up systems with lower gradients, post processing of the pose estimations using a Kalman filter could be considered [25] in order to improve the precision, especially close to the edges of the workspace where the precision is lower.

Using our phasor field prediction method based on a single reference sensor we estimated the influence of the actuation currents on the localization fields and measured a mean accuracy of 0.35 mm throughout the workspace that increased to 0.6mm when applying actuation fields up to 10 mT at the center of the workspace. More advanced methods for modelling the influence of the actuation currents [1] could be explored in the future to further improve the accuracy of the method with stronger actuation fields.

Both the accuracy and the precision of the method are expected to scale linearly with the length scale of the eMNS, assuming that oscillating fields of the same amplitude would be generated throughout the workspace of the scaled system. This follows from the fact that the error in position estimation is inversely proportional to the localization field gradients as discussed in Appendix C-C and section III-G.

The method presented in this paper requires the transmission of reactive power to the electromagnets by application of an oscillatory voltage. For the system in this paper, a maximum of 22 V needed to be applied to drive the localization currents of 0.4 A and transmit a maximum of 220 VAr to the electromagnet at the point of highest actuation current. We discussed the scaling of these quantities and showed the feasibility of a scaled system implementing our method.

We proposed methods to compensate for both the non-linear response of the electromagnets and their dynamic behaviour, making our method generic, model-free, and applicable to a broad variety of eMNS. For these reasons, we believe this approach constitutes a contribution that can help advance the clinical adoption of RMN in minimally invasive surgery in the future.

APPENDIX A
ESTIMATION OF ACTUATION FIELD

In (12), an estimate of the actuation field sequence was introduced by representing each of the three estimated actuation field sequences ${}^{\mathbf{c}_i}\hat{\boldsymbol{\mathcal{B}}}^{\mathrm{a}}_{s_i}$ as a sum of base sequences

$$ {}^{\mathbf{c}_i}\hat{\boldsymbol{\mathcal{B}}}^{\mathrm{a}}_{s_i} = \sum_h c_{i,h} \boldsymbol{f}^{\mathrm{a}}_h $$

where $c_{i,h}$ are the components of the coefficient vector $\mathbf{c}_i \in \mathbb{R}^H$. These coefficients were chosen in (13) such that the DFT of the estimated actuation field closely matches the DFT of the measured magnetic field at all discrete frequencies except k_m and $N_s - k_m$. Introducing the shorthand notation $\check{\mathbf{x}} := \mathcal{F}(\mathbf{x})_{k \neq k_m} \in \mathbb{C}^{N_s - 2M}$ for the DFT of a vector $\mathbf{x} \in \mathbb{R}^{N_s}$ with the entries k_m and $N_s - k_m$ omitted, the square of the objective function to be minimized in (13) can be written as

$$ o(\mathbf{c}_i) = \left\langle \check{\boldsymbol{\mathcal{B}}}_{s_i} - \sum_{h'} c_{i,h'} \check{\boldsymbol{f}}^{\mathrm{a}}_{h'} \, , \, \check{\boldsymbol{\mathcal{B}}}_{s_i} - \sum_{h'} c_{i,h'} \check{\boldsymbol{f}}^{\mathrm{a}}_{h'} \right\rangle $$

where $\langle \cdot, \cdot \rangle$ denotes the standard inner product of $\mathbb{C}^{N_s - 2M}$. The minimization of o requires that

$$ \frac{\partial o}{\partial c_{i,h}} = -2 \operatorname{Re} \left\langle \check{\boldsymbol{f}}^{\mathrm{a}}_h \, , \, \check{\boldsymbol{\mathcal{B}}}_{s_i} - \sum_{h'} c_{i,h'} \check{\boldsymbol{f}}^{\mathrm{a}}_{h'} \right\rangle = 0 $$

This equation can be rearranged to the following form:

$$ \left[\operatorname{Re} \left(\langle \check{\boldsymbol{f}}^{\mathrm{a}}_h, \check{\boldsymbol{\mathcal{B}}}_{s_i} \rangle \right) \right] = \left[\operatorname{Re} \left(\langle \check{\boldsymbol{f}}^{\mathrm{a}}_h \, , \, \check{\boldsymbol{f}}^{\mathrm{a}}_{h'} \rangle \right) \right] \mathbf{c}_i $$

which is a linear system that can be solved for the coefficient vector $\mathbf{c}_i$.

APPENDIX B
ORIENTATION ESTIMATION PROCEDURE AS A WEIGHTED ORTHOGONAL PROCRUSTES PROBLEM FOR COMPLEX MATRICES

Algorithm 1 was introduced to estimate the orientation of the sensor by solving the weighted orthogonal Procrustes problem, which minimizes (19) for both the rotation matrix $\mathbf{R}$ and the weighting matrix $\mathbf{W}$. The algorithm iteratively applies the two solution steps detailed below in order to minimize the objective function of the form

$$ \| \mathbf{RAW} - \mathbf{B} \|_F \tag{29} $$

for $\mathbf{R} \in SO(3)$ and $\mathbf{W} = \operatorname{diag}(w_1, \cdots, w_M) \in \mathbb{C}^{M \times M}$, with complex matrices $\mathbf{A}, \mathbf{B} \in \mathbb{C}^{3 \times M}$.

A. Step 1: rotation matrix estimation

The first step consists of computing the rotation matrix $\mathbf{R}$, which minimizes (29) for a given guess of the weighting matrix $\mathbf{W}$. This consists of solving an orthogonal Procrustes problem for complex matrices. The derivation presented here is based on [26] but takes into account the fact that the matrices $\mathbf{C} := \mathbf{AW}$ and $\mathbf{B}$ are complex-valued. The square of the objective function to be minimized is written as

$$ \begin{aligned} \| \mathbf{RC} - \mathbf{B} \|_F^2 &= \operatorname{tr}\big((\mathbf{RC} - \mathbf{B})^H (\mathbf{RC} - \mathbf{B}) \big) \\ &= \operatorname{tr}\big(\mathbf{C}^H \mathbf{C} + \mathbf{B}^H \mathbf{B} - \mathbf{B}^H \mathbf{RC} - (\mathbf{RC})^H \mathbf{B} \big) \\ &= \operatorname{tr}\big(\mathbf{C}^H \mathbf{C} + \mathbf{B}^H \mathbf{B} - 2 \operatorname{Re}(\mathbf{B}^H \mathbf{RC}) \big) \end{aligned} $$

where $\mathbf{M}^H$ denotes the conjugate transpose of a matrix $\mathbf{M}$. Only the last term depends on $\mathbf{R}$, so minimizing the objective function is equivalent to maximizing the following expression:

$$ \operatorname{tr}\big(\operatorname{Re}(\mathbf{B}^H \mathbf{RC}) \big) = \operatorname{tr}\big(\mathbf{R} \operatorname{Re}(\mathbf{CB}^H) \big) $$

which is maximized by choosing $\mathbf{R}$ as [26]

$$ \hat{\mathbf{R}} = \mathbf{V} \operatorname{diag}(1, 1, \det\big(\mathbf{UV}^T\big)) \mathbf{U}^T \tag{30} $$

with the singular value decomposition

$$ \mathbf{U \Sigma V}^T = \operatorname{Re}(\mathbf{CB}^H) = \operatorname{Re}((\mathbf{AW})\mathbf{B}^H) $$

B. Step 2: weighting matrix estimation

The second step consists of computing the weighting matrix $\mathbf{W}$, which minimizes (29) for a the given estimate $\hat{\mathbf{R}}$ of the rotation matrix determined in the first step. The square of the objective function can be written in the following way with $\mathbf{D} := \hat{\mathbf{R}}\mathbf{A}$

$$\begin{aligned}\|\mathbf{DW}-\mathbf{B}\|_F^2 &= \mathrm{tr}\big((\mathbf{DW}-\mathbf{B})^H(\mathbf{DW}-\mathbf{B})\big)\\ &= \mathrm{tr}\big(\mathbf{W}^H\mathbf{D}^H\mathbf{DW}-\mathbf{B}^H\mathbf{DW}-(\mathbf{DW})^H\mathbf{B}\big)\\ &\quad+\mathrm{tr}\big(\mathbf{B}^H\mathbf{B}\big)\\ &= \mathrm{tr}\big(\mathbf{W}^H\mathbf{D}^H\mathbf{DW}-2\,\mathrm{Re}(\mathbf{B}^H\mathbf{DW})+\mathbf{B}^H\mathbf{B}\big)\end{aligned}$$

Its value is a quadratic function of the weights determined by the first two terms of the last expression. These can be rewritten as

$$\sum_i x_i|w_i|^2 - 2\,\mathrm{Re}\left(\sum_i y_i w_i\right) \tag{31}$$

with x_i the diagonal elements of $\mathbf{X} := \mathbf{D}^H\mathbf{D} = \mathbf{A}^H\mathbf{A}$ and y_i the diagonal elements of $\mathbf{Y} := \mathbf{B}^H\mathbf{D} = \mathbf{B}^H\hat{\mathbf{R}}\mathbf{A}$. Let us denote $w_i := a_i + jb_i$, the expression (31) becomes

$$\sum_i x_i\left(a_i^2+b_i^2\right) - 2\left(a_i\,\mathrm{Re}(y_i) - b_i\,\mathrm{Im}(y_i)\right) \tag{32}$$

The sum (32) can be minimized for a_i and b_i, resulting in the optimal weights

$$w_i = \frac{\mathrm{Re}(y_i) - j\,\mathrm{Im}(y_i)}{x_i} = \frac{\mathbf{Y}[i,i]^*}{\mathbf{X}[i,i]}$$

where * denotes the complex conjugate.

APPENDIX C
PRECISION OF LOCALIZATION METHOD

In this appendix, it is shown that the intrinsic noise of the Hall effect sensor characterized by the standard deviation σ_{Hall} causes a position estimation noise with standard deviation $\sigma_{\hat{p}_i}$ as stated in (22):

$$\sigma_{\hat{p}_i} = \frac{\sigma_{\mathrm{Hall}}}{\sqrt{2N_s}}\sqrt{\sum_m\left(\frac{\partial|\underline{\mathbf{b}}_m|}{\partial p_i}\bigg|_{\mathbf{p}}\right)^{-2}} = \frac{\sigma_{\mathrm{Hall}}}{\sqrt{2N_s}}g_i(\mathbf{p})^{-1}$$

A. Noise on phasors

Consider the estimation of a phasor using the DFT according to (10). Consider $\boldsymbol{n} \in \mathbb{R}^{N_s}$ to be the noise of the Hall sensor in a noisy measurement sequence $\tilde{\boldsymbol{\mathcal{b}}}_{s_i}$ such that $\tilde{\boldsymbol{\mathcal{b}}}_{s_i} = \boldsymbol{\mathcal{b}}_{s_i} + \boldsymbol{n}$ where $\boldsymbol{\mathcal{b}}_{s_i}$ is an ideal, noiseless measurement sequence (Fig. 15a). The Hall sensor noise results in a random noise phasor $\underline{n}$ being added to the measurement of the phasor $\underline{b}_{m,s_i}$ (Fig. 15b). We can think of $\underline{n}$ as a complex valued random variable. If we assume that the Hall sensor noise is white, the variance of $\underline{n}$ is given by $\sigma_{\mathrm{Hall}}^2/N_s$ due to Parsevals theorem (for the sake of simplicity, we assume that the noise in all three directions is the same for the Hall sensor). We can think of the random noise phasor as having two independent components, one in the direction of $\underline{b}_{m,s_i}$ and one perpendicular such that $\underline{n} = d\underline{e}_d + q\underline{e}_q$ where $\underline{e}_d$ and $\underline{e}_q$ are local unit phasors (Fig. 15b) and d and q are real valued random variables. Both orthogonal noise components are independent and contribute equally to the variance of $\underline{n}$ such that

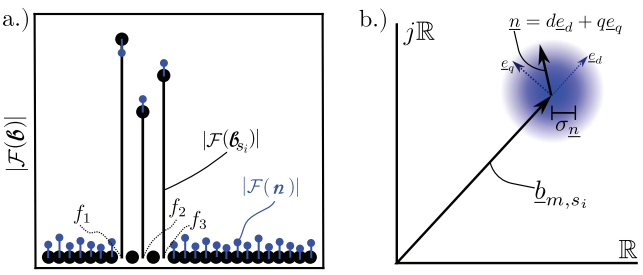

Fig. 15. a.) Noise measurement sequence $\boldsymbol{n}$ added on Hall measurement sequence $\boldsymbol{\mathcal{b}}_{s_i}$ b.) Random noise phasor $\underline{n}$ added on noiseless phasor measurement $\underline{b}_{m,s_i}$

$$\sigma_{\underline{n}}^2 = \sigma_d^2 + \sigma_q^2 = \frac{\sigma_{\mathrm{Hall}}^2}{N_s} \tag{33}$$

We consider how the noise phasor $\underline{n}$ affects the measurement of the phasor magnitude $|\underline{b}_{m,s_i}|$ which is used to localize the sensor:

$$\tilde{|\underline{b}_{m,s_i}|} = \sqrt{(|\underline{b}_{m,s_i}|+d)^2+q^2} \approx |\underline{b}_{m,s_i}| + d \tag{34}$$

In the above equation, $\tilde{|\underline{b}_{m,s_i}|}$ is the noisy magnitude estimate and we assumed $d, q \ll |\underline{b}_{m,s_i}|$ and linearized the expression around $|\underline{b}_{m,s_i}|$. From the above equation, it is seen that only the noise component in direction of the phasor (d-component) contributes noise to the phasor magnitude measurement.

B. Noise on phasor vector magnitudes

The noisy measurement of the magnetic field phasor vector magnitude is given by

$$\tilde{|\underline{\mathbf{b}}_m|} = \sqrt{|\underline{b}_{m,s_1}+\underline{n}_1|^2 + |\underline{b}_{m,s_2}+\underline{n}_2|^2 + |\underline{b}_{m,s_3}+\underline{n}_3|^2}$$

where $\underline{n}_1, \underline{n}_2, \underline{n}_3$ describe the noise phasors on the components of $\underline{\mathbf{b}}_m$. As we assume that the noise is small relative to the phasor quantities, the above expression can be linearized as follows:

$$\tilde{|\underline{\mathbf{b}}_m|} = |\underline{\mathbf{b}}_m| + \frac{|\underline{b}_{m,s_1}|}{|\underline{\mathbf{b}}_m|}d_1 + \frac{|\underline{b}_{m,s_2}|}{|\underline{\mathbf{b}}_m|}d_2 + \frac{|\underline{b}_{m,s_3}|}{|\underline{\mathbf{b}}_m|}d_3 \tag{35}$$

again assuming that only the d-components of the phasor noise contributes to the magnitude measurement (Eq. (34)). The random variables d_1, d_2, d_3 in (35) are independent and therefore, we can write for the variance $\sigma^2_{|\underline{\mathbf{b}}_m|}$:

$$\begin{aligned}\sigma^2_{|\underline{\mathbf{b}}_m|} &= \left(\frac{|\underline{b}_{m,s_1}|}{|\underline{\mathbf{b}}_m|}\right)^2\sigma_d^2 + \left(\frac{|\underline{b}_{m,s_2}|}{|\underline{\mathbf{b}}_m|}\right)^2\sigma_d^2 + \left(\frac{|\underline{b}_{m,s_3}|}{|\underline{\mathbf{b}}_m|}\right)^2\sigma_d^2\\ &= \sigma_d^2 = \frac{\sigma_{\mathrm{Hall}}^2}{2N_s}\end{aligned}$$

C. Position estimation noise

In order to see how the noise on the phasor vector magnitudes $|\underline{\mathbf{b}}_m|$ affects position estimation we consider (17) which is used to estimate the position:

$$\hat{\mathbf{p}} = \underset{\mathbf{p}}{\mathrm{argmin}}\sum_m\left(|\hat{\underline{\mathbf{b}}}_m| - \tilde{|\underline{\mathbf{b}}_m|}(\mathbf{p},\mathbf{i}^{\mathrm{a}})\right)^2$$

We assume that the phasor magnitude field estimate is perfect, i.e. $|\breve{\underline{\mathbf{b}}}_m|(\mathbf{p}, \mathbf{i}^{\mathrm{a}}) = |\underline{\mathbf{b}}_m|(\mathbf{p}, \mathbf{i}^{\mathrm{a}})$. We also assume again that the phasor noise introduces random, independent errors ϵ_m with variance $\sigma^2_{|\underline{\mathbf{b}}_m|}$ in the magnitude measurements of the phasor vectors so that $|\hat{\underline{\mathbf{b}}}_m| = |\underline{\mathbf{b}}_m|(\mathbf{p}_0, \mathbf{i}^{\mathrm{a}}) + \epsilon_m$. Linearizing the objective function around the sensor position $\mathbf{p}_0$ and solving the resulting linear system leads to

$$\hat{\mathbf{p}} = \mathbf{p}_0 + \left[\frac{\partial \mathbf{p}}{\partial |\underline{\mathbf{b}}_m|}\right] [\epsilon_1 \cdots \epsilon_M]^T \tag{36}$$

with $\left[\frac{\partial \mathbf{p}}{\partial |\underline{\mathbf{b}}_m|}\right] \in \mathbb{R}^{3\times M}$ the inverse Jacobian of the magnetic phasor magnitude field. Given the properties of the random errors ϵ_m, we can write for the variance of the position estimate in direction $\mathbf{e}_i$:

$$\begin{aligned}\sigma^2_{\hat{p}_i} &= \sigma^2_{|\underline{\mathbf{b}}_m|} \sum_m \left(\frac{\partial p_i}{\partial |\underline{\mathbf{b}}_m|}\right)^2 \\ &= \frac{\sigma^2_{\mathrm{Hall}}}{2N_s} \sum_m \left(\frac{\partial |\underline{\mathbf{b}}_m|}{\partial p_i}\right)^{-2}\end{aligned}$$

from which (22) follows.

ACKNOWLEDGMENT

This work was supported by the Swiss National Science Foundation through grant number 200020B_185039 and 20B2-1_180861, the ITC-InnoHK funding, the European Union's Horizon 2020 Proactive Open program under grant agreement No 952152, the ERC Advanced Grant 743217 Soft Micro Robotics (SOMBOT), and the ERC Consolidator Grant 771565 (HINBOTS).

REFERENCES

[1] S. L. Charreyron, Q. Boehler, B. Kim, C. Weibel, C. Chautems, and B. J. Nelson, "Modeling electromagnetic navigation systems," *IEEE Transactions on Robotics*, vol. 37, no. 4, pp. 1009–1021, 2021.

[2] I. Tunay, "Position control of catheters using magnetic fields," in *Proceedings of the IEEE International Conference on Mechatronics, 2004. ICM '04.*, 2004, pp. 392–397.

[3] C. Heunis, J. Sikorski, and S. Misra, "Flexible instruments for endovascular interventions: Improved magnetic steering, actuation, and image-guided surgical instruments," *IEEE Robotics & Automation Magazine*, vol. 25, no. 3, pp. 71–82, 2018.

[4] Y. Kim, E. Genevriere, P. Harker, J. Choe, M. Balicki, R. W. Regenhardt, J. E. Vranic, A. A. Dmytriw, A. B. Patel, and X. Zhao, "Telerobotic neurovascular interventions with magnetic manipulation," *Science Robotics*, vol. 7, no. 65, p. eabg9907, Apr. 2022. [Online]. Available: https://www.science.org/doi/10.1126/scirobotics.abg9907

[5] A. Hong, A. J. Petruska, A. Zemmar, and B. J. Nelson, "Magnetic control of a flexible needle in neurosurgery," *IEEE Transactions on Biomedical Engineering*, vol. 68, no. 2, pp. 616–627, 2021.

[6] D. Son, M. C. Ugurlu, and M. Sitti, "Permanent magnet array–driven navigation of wireless millirobots inside soft tissues," *Science Advances*, vol. 7, no. 43, p. eabi8932, Oct. 2021. [Online]. Available: https://www.science.org/doi/10.1126/sciadv.abi8932

[7] S. Sharma, A. Telikicherla, G. Ding, F. Aghlmand, A. H. Talkhooncheh, M. G. Shapiro, and A. Emami, "Wireless 3d surgical navigation and tracking system with 100um accuracy using magnetic-field gradient-based localization," *IEEE Transactions on Medical Imaging*, vol. 40, no. 8, pp. 2066–2079, 2021.

[8] C. Vergne, C. Féry, T. Quirin, H. Nicolas, M. Madec, S. Hemm, and J. Pascal, "Low-field electromagnetic tracking using 3-d magnetometer for assisted surgery," *IEEE Transactions on Magnetics*, vol. 59, no. 2, pp. 1–5, 2023.

[9] S. Sharma, K. B. Ramadi, N. H. Poole, S. S. Srinivasan, K. Ishida, J. Kuosmanen, J. Jenkins, F. Aghlmand, M. B. Swift, M. G. Shapiro, G. Traverso, and A. Emami, "Location-aware ingestible microdevices for wireless monitoring of gastrointestinal dynamics," *Nature Electronics*, Feb. 2023. [Online]. Available: https://www.nature.com/articles/s41928-023-00916-0

[10] C. Di Natali, M. Beccani, and P. Valdastri, "Real-time pose detection for magnetic medical devices," *IEEE Transactions on Magnetics*, vol. 49, no. 7, pp. 3524–3527, 2013.

[11] C. Di Natali, M. Beccani, N. Simaan, and P. Valdastri, "Jacobian-based iterative method for magnetic localization in robotic capsule endoscopy," *IEEE Transactions on Robotics*, vol. 32, no. 2, pp. 327–338, 2016.

[12] K. M. Popek, T. Schmid, and J. J. Abbott, "Six-degree-of-freedom localization of an untethered magnetic capsule using a single rotating magnetic dipole," *IEEE Robotics and Automation Letters*, vol. 2, no. 1, pp. 305–312, 2017.

[13] T. da Veiga, G. Pittiglio, M. Brockdorff, J. H. Chandler, and P. Valdastri, "Six-degree-of-freedom localization under multiple permanent magnets actuation," *IEEE Robotics and Automation Letters*, vol. 8, no. 6, pp. 3422–3429, 2023.

[14] A. J. Sperry, J. J. Christensen, and J. J. Abbott, "Six-degree-of-freedom localization with a 3-axis accelerometer and a 2-axis magnetometer for magnetic capsule endoscopy," *IEEE Robotics and Automation Letters*, vol. 7, no. 2, pp. 2110–2115, 2022.

[15] A. Z. Taddese, P. R. Slawinski, M. Pirotta, E. D. Momi, K. L. Obstein, and P. Valdastri, "Enhanced real-time pose estimation for closed-loop robotic manipulation of magnetically actuated capsule endoscopes," *The International Journal of Robotics Research*, vol. 37, no. 8, pp. 890–911, 2018. [Online]. Available: https://doi.org/10.1177/0278364918779132

[16] D. Son, S. Yim, and M. Sitti, "A 5-d localization method for a magnetically manipulated untethered robot using a 2-d array of hall-effect sensors," *IEEE/ASME Transactions on Mechatronics*, vol. 21, no. 2, pp. 708–716, 2016.

[17] D. Son, M. D. Dogan, and M. Sitti, "Magnetically actuated soft capsule endoscope for fine-needle aspiration biopsy," in *2017 IEEE International Conference on Robotics and Automation (ICRA)*. IEEE, 2017, pp. 1132–1139.

[18] Y. Kim, G. A. Parada, S. Liu, and X. Zhao, "Ferromagnetic soft continuum robots," *Science Robotics*, vol. 4, no. 33, p. eaax7329, 2019.

[19] C. Fischer, Q. Boehler, and B. J. Nelson, "Using magnetic fields to navigate and simultaneously localize catheters in endoluminal environments," *IEEE Robotics and Automation Letters*, vol. 7, no. 3, pp. 7217–7223, 2022.

[20] C. Fischer, T. Quirin, C. Chautems, Q. Boehler, J. Pascal, and B. J. Nelson, "Gradiometer-based magnetic localization for medical tools," *IEEE Transactions on Magnetics*, vol. 59, no. 2, pp. 1–5, 2023.

[21] M. P. Kummer, J. J. Abbott, B. E. Kratochvil, R. Borer, A. Sengul, and B. J. Nelson, "Octomag: An electromagnetic system for 5-dof wireless micromanipulation," *IEEE Transactions on Robotics*, vol. 26, no. 6, pp. 1006–1017, 2010.

[22] S. Schuerle, S. Erni, M. Flink, B. E. Kratochvil, and B. J. Nelson, "Three-dimensional magnetic manipulation of micro- and nanostructures for applications in life sciences," *IEEE Transactions on Magnetics*, vol. 49, no. 1, pp. 321–330, 2013.

[23] J. C. Gower and G. B. Dijksterhuis, "Orthogonal Procrustes problems," in *Procrustes Problems*. Oxford University Press, 01 2004, ch. 4.6.1, pp. 100–102. [Online]. Available: https://doi.org/10.1093/acprof:oso/9780198510581.003.0004

[24] D. Q. Huynh, "Metrics for 3D Rotations: Comparison and Analysis," *Journal of Mathematical Imaging and Vision*, vol. 35, no. 2, pp. 155–164, Oct. 2009. [Online]. Available: http://link.springer.com/10.1007/s10851-009-0161-2

[25] A. Dore, G. Smoljkic, E. V. Poorten, M. Sette, J. V. Sloten, and G.-Z. Yang, "Catheter navigation based on probabilistic fusion of electromagnetic tracking and physically-based simulation," in *2012 IEEE/RSJ International Conference on Intelligent Robots and Systems*, 2012, pp. 3806–3811.

[26] S. Ahmed and I. M. Jaimoukha, "A relaxation-based approach for the orthogonal procrustes problem with data uncertainties," in *Proceedings of 2012 UKACC International Conference on Control*, 2012, pp. 906–911.

Denis von Arx received the BSc and MSc degrees in electrical engineering from ETH Zurich in 2016 and 2018. He joined the Multi Scale Robotics Lab at ETH Zurich in 2019 to work on electromagnetic actuation systems. He is currently working toward the Ph.D. degree at MSRL. His research interests include electromagnetic actuation and localization.

Cedric Fischer received the BSc and MSc degrees in mechanical engineering from ETH Zurich in 2014 and 2017. In 2018 he joined the Multi Scale Robotics Lab at the Institute of Robotics and Intelligent Systems at ETH Zurich as a Ph.D. candidate. His current research includes the modelling of electromagnetic navigation systems and the development of magnetic localization methods for minimally invasive surgery.

Harun Torlakcik received the BSc and MSc degrees in mechanical engineering from ETH Zurich. In 2018 he joined the Multi Scale Robotics Lab at the Institute of Robotics and Intelligent Systems at ETH to work towards the Ph.D. degree. His current research includes the development and control of magnetically guided micro- and nanorobots for biomedical applications, including targeted drug delivery, wound healing and cell differentiation.

Salvador Pané Salvador Pané is a Professor of Materials for Robotics and Codirector of the Multi-Scale Robotics Lab (MSRL) at the ETH Zürich. He received his Ph.D. in Chemistry from the University of Barcelona in 2008 and subsequently joined MSRL as a Postdoctoral Researcher in August 2008. He has been awarded the highly competitive ERC-Starting Grant (StG) and ERCConsolidator Grant (CoG) in 2012 and 2017, respectively. Since 2023, he is elected member of the Institut d'Estudis Catalans in the section of Science and Technology. His interests lie in bridging materials science, chemistry, and electrochemistry with small-scale robotics for various applications.

Bradley J. Nelson Brad Nelson (M'90, SM'06, F'11) received the B.S. degree in Mechanical Engineering from the University of Illinois at Urbana-Champaign in 1984, the M.S. degree in Mechanical Engineering from the University of Minnesota in 1987, and the Ph.D. degree in Robotics from the School of Computer Science, Carnegie-Mellon University, Pittsburgh, PA, in 1995. He has been the Professor of Robotics and Intelligent Systems at ETH Zürich since 2002, where his research focuses on micro and nanorobotics with applications in biology and medicine. He has received a number of awards for his work in robotics, nanotechnology, and biomedicine.

Quentin Boehler Quentin Boehler received a master's degree in mechatronics from INSA Strasbourg, France in 2013, and a Ph.D. degree in robotics from the University of Strasbourg, France in 2016. He joined the Multi-Scale Robotics Lab at ETH Zurich in 2017 and is currently a senior scientist. His research interests include magnetic actuation for medical robotics, the development and analysis of electromagnetic navigation systems, and the design and control of robotic systems for minimally invasive surgery.

IEEE Transactions on Robotics (T-RO) paper, presented at ICRA 2024, Yokohama, Japan. Cite as T-RO paper.